A Survey of Protoplanetary Disks Using the Keck/NIRC2 Vortex Coronagraph

Nicole L. Wallack[1,2], Jean-Baptiste Ruffio[3], Garreth Ruane[4], Bin B. Ren (任彬)[5,6,7,31], Jerry W. Xuan[5], Marion Villenave[4,8], Dimitri Mawet[5,4], Karl Stapelfeldt[4], Jason J. Wang[5,9], Michael C. Liu[10], Olivier Absil[11], Carlos Alvarez[12], Jaehan Bae[1,13], Charlotte Bond[14], Michael Bottom[10], Benjamin Calvin[5,15], Élodie Choquet[16], Valentin Christiaens[11], Therese Cook[15], Bruno Femenía Castellá[17,18], Carlos Gomez Gonzalez[19], Greta Guidi[20], Elsa Huby[21], Joel Kastner[22,23,24], Heather A. Knutson[2], Tiffany Meshkat[25], Henry Ngo[26], Sam Ragland[12], Maddalena Reggiani[27], Luca Ricci[28], Eugene Serabyn[4], Taichi Uyama[25], Jonathan P. Williams[10], Peter Wizinowich[12], Zoe Zawol[5], Shangjia Zhang[29,30], and Zhaohuan Zhu[29,30]

[1] Earth and Planets Laboratory, Carnegie Institution for Science, Washington, DC 20015, USA; nwallack@carnegiescience.edu
[2] Division of Geological & Planetary Sciences, California Institute of Technology, MC 150-21, Pasadena, CA 91125, USA
[3] Department of Astronomy & Astrophysics, University of California, San Diego, La Jolla, CA 92093, USA
[4] Jet Propulsion Laboratory, California Institute of Technology, 4800 Oak Grove Drive, Pasadena, CA, 91109, USA
[5] Department of Astronomy, California Institute of Technology, MC 249-17, 1200 East California Boulevard, Pasadena, CA 91125, USA
[6] Université Côte d'Azur, Observatoire de la Côte d'Azur, CNRS, Laboratoire Lagrange, Bd de l'Observatoire, CS 34229, 06304 Nice cedex 4, France
[7] Université Grenoble Alpes, Institut de Planétologie et d'Astrophysique (IPAG), F-38000 Grenoble, France
[8] Università degli Studi di Milano, Dipartimento di Fisica, via Celoria 16, 20133 Milano, Italy
[9] Center for Interdisciplinary Exploration and Research in Astrophysics (CIERA) and Department of Physics and Astronomy, Northwestern University, Evanston, IL 60208, USA
[10] Institute for Astronomy, University of Hawaii, 2680 Woodlawn Drive, Honolulu, HI 96822, USA
[11] STAR Institute, Université de Liège, 19c Allée du Six Août, 4000 Liège, Belgium
[12] W. M. Keck Observatory, Kamuela, HI, USA
[13] Department of Astronomy, University of Florida, Gainesville, FL 32611, USA
[14] Science and Technology Facilities Council (STFC), Polaris House, North Star Avenue, Swindon, SN2 1SZ, UK
[15] Department of Physics & Astronomy, University of California Los Angeles, Los Angeles, CA 90095, USA
[16] Aix Marseille Univ, CNRS, CNES, LAM, Marseille, France
[17] Instituto de Astrofísica de Canarias, C/ Vía Láctea s/n, E-38205 San Cristóbal de la Laguna, Spain
[18] Departamento de Astrofísica, Universidad de La Laguna, E-38205 San Cristóbal de la Laguna, Spain
[19] Centre Nacional de Supercomputació, Plaça d'Eusebi Güell, 1-3, 08034 Barcelona, Spain
[20] Institut de Radio Astronomie Millimétrique (IRAM), 300 rue de la Piscine, 38406 Saint Martin d'Hères, France
[21] LESIA, Observatoire de Paris, Université PSL, CNRS, Sorbonne Université, Université de Paris Cité, 5 place Jules Janssen, 92195 Meudon, France
[22] Center for Imaging Science, Rochester Institute of Technology, Rochester, NY 14623, USA
[23] School of Physics and Astronomy, Rochester Institute of Technology, Rochester, NY 14623, USA
[24] Laboratory for Multiwavelength Astrophysics, Rochester Institute of Technology, Rochester, NY 14623, USA
[25] IPAC, California Institute of Technology, M/C 100-22, 1200 East California Boulevard, Pasadena, CA 91125, USA
[26] NRC Herzberg Astronomy and Astrophysics, 5071 West Saanich Road, Victoria, British Columbia, Canada
[27] Institute of Astronomy, KU Leuven, Celestijnenlaan 200D, B-3001 Leuven, Belgium
[28] Department of Physics and Astronomy, California State University Northridge, 18111 Nordhoff Street, Northridge, CA 91130, USA
[29] Nevada Center for Astrophysics, University of Nevada, Las Vegas, 4505 S. Maryland Parkway, Las Vegas, NV 89154, USA
[30] Department of Physics and Astronomy, University of Nevada, Las Vegas, 4505 S. Maryland Parkway, Las Vegas, NV 89154, USA

Abstract

Recent Atacama Large Millimeter/submillimeter Array (ALMA) observations of protoplanetary disks in the millimeter continuum have shown a variety of radial gaps, cavities, and spiral features. These substructures may be signposts for ongoing planet formation, and therefore these systems are promising targets for direct imaging planet searches in the near-infrared. To this end, we present results from a deep imaging survey in the L' band (3.8 μm) with the Keck/NIRC2 vortex coronagraph to search for young planets in 43 disks with resolved features in the millimeter continuum or evidence for gaps/central cavities from their spectral energy distributions. Although we do not detect any new point sources, using the vortex coronagraph allows for high sensitivity to faint sources at small angular separations (down to $\sim0\rlap{.}''1$), allowing us to place strong upper limits on the masses of potential gas giant planets. We compare our mass sensitivities to the masses of planets derived using ALMA observations, and while we are sensitive to $\sim1\ M_{\rm Jup}$ planets in the gaps in some of our systems, we are generally not sensitive to planets of the masses expected from the ALMA observations. In addition to placing upper limits on the masses of gas giant planets that could be interacting with the dust in the disks to form the observed millimeter substructures, we are also able to map the micron-sized dust as seen in scattered light for 8 of these systems. Our large sample of systems also allows us to investigate limits on planetary accretion rates and disk viscosities.

---

[31] Marie Skłodowska-Curie Fellow.

1. Introduction

Gaps, cavities, and spiral features seen in protoplanetary disks are thought to be the signposts of planet formation. Millimeter-sized dust grains are expected to rapidly drift inward, resulting in the depletion of large dust grains at large

radii (Weidenschilling 1977). However, when imaged by facilities such as the Atacama Large Millimeter/submillimeter Array (ALMA), structures in the large dust grains are evident out to hundreds of astronomical units in many protoplanetary disks (e.g., Andrews et al. 2018; Long et al. 2018). In order to keep these dust grains at such large orbital separations, there must be mechanisms in effect that trap dust grains at large distances and produce the spiral, concentric ring, and gap substructures that seem to be prevalent among protoplanetary disks imaged with ALMA. A number of different mechanisms have been suggested to explain the protoplanetary disk dust distributions, including magnetorotational instabilities, dead zones, and condensation fronts (e.g., Isella et al. 2016; Liu et al. 2018; Ohashi & Kataoka 2019). However, one of the most favored explanations for the substructures in the observed millimeter dust in these disks is that they are caused by forming planets interacting with the natal disk structure. Forming giant planets can cause pressure bumps outside of their orbits and trap large dust grains into rings while less massive planets generally open gaps in the dust in the disks with no significant changes to the local gas (Paardekooper & Mellema 2006; Zhu et al. 2014). The presence of protoplanets associated with disk substructures has also been inferred by measuring deviations from the Keplerian velocity in the gas velocity field (Teague et al. 2018; Pinte et al. 2019).

Determining the masses of the planets that are carving out the gaps in the gas and dust of the disk is complicated by uncertainties in the bulk disk parameters, which can lead to large degeneracies in the masses derived from the geometries of millimeter dust cavities and gaps. For example, assuming different values for the disk viscosity, which is a largely observationally unconstrained parameter, can lead to differences in the calculated masses of planets on the order of a factor of >4 (Zhang et al. 2018). One way to more directly estimate the masses of planets carving these gaps is to directly detect the young planets' thermal emission.

Direct imaging is uniquely able among planet detection and characterization methods to probe the locations of the proposed wide-separation planets carving out the gaps in these young systems. Thus, direct imaging is capable of detecting planets in the act of forming, allowing us to place observational constraints on the masses required to carve out millimeter gaps and also on formation locations and accretion timescales. Leveraging the fact that both the blackbody expectation and predictions from more rigorous atmospheric models (Skemer et al. 2014) of a cool planet would dictate more advantageous contrast in the L' band (3.8 μm) over other wavelengths, there have been multiple direct imaging surveys of protoplanetary disks at L' (e.g., Stone et al. 2018; Launhardt et al. 2020; Cugno et al. 2023) and more broadly in the infrared (Asensio-Torres et al. 2021). Moreover, observing in the L' band allows for a compromise between more favorable planet-to-star contrast expectations and increased background noise at longer infrared wavelengths such as the M band.

Conducting a survey at L' also allows for more advantageous planet-to-star flux ratios over millimeter wavelengths making these infrared surveys the most sensitive to directly detecting the planets inferred by the millimeter data. Additionally, infrared wavelength observations also provide information on the micron-sized dust distribution as inferred from scattered light. This means that this technique allows for both possible direct detection of planets while also providing a better understanding of the distribution of small dust grains, allowing for direct observations of planets interacting with their natal disks and actively accreting their atmospheres (e.g., the PDS 70 system; Benisty et al. 2018; Keppler et al. 2018).

To this end, we present a survey using the Keck/NIRC2 vortex coronagraph (Mawet et al. 2017; Serabyn et al. 2017) of protoplanetary disks previously observed at other wavelengths that show substructures and/or cavities. Utilizing the vortex coronagraph allows for high sensitivity to faint sources at small angular separations (down to 0″.1), ideal for probing the cavities shown in the millimeter/submillimeter dust close to the host stars.

However, owing to our sample of systems being comprised of those with known disk structure, an important caveat to our sensitivity to planets is that the effects of extinction from the circumstellar disks can also lead to uncertainties in the derived planet masses. Using hydrodynamic simulations, Sanchis et al. (2020) found extinction coefficients, A_L, for a 2 $M_{\rm Jup}$ planet at 100 au to be 1.31 and for a 5 $M_{\rm Jup}$ planet at the same location to be 0.02. Moreover, determining the exact level of the extinction caused by the circumstellar disk in these systems is nontrivial, and indeed the values of the extinction are dependent on the surface densities of the gas and dust (Cugno et al. 2023). Therefore, the masses derived from direct imaging in the infrared, while more directly estimated than using the geometries of the dust and gas at millimeter wavelengths, come with the large caveat that extinction, and the uncertainties on extinction, may alter the derived values.

In Section 2 we discuss the strategy for our observations. In Section 3, we present the detection limits of all our targets using our derived contrast curves, and in Section 4 we put these contrast curves into the broader context of the detection possibility of long-period giant planets.

2. Observations

2.1. Target Selection

All targets were selected using the criteria that (1) there are published images in the millimeter/submillimeter or a published spectral energy distribution (SED); (2) they show evidence in the ALMA data or SED for a gap and/or cavity that could have been formed due to interactions between the millimeter-sized dust and a forming protoplanet; (3) they are nearby (preferably within ~300 pc); (4) they are bright enough for a high-quality adaptive optics (AO) correction; and (5) they are estimated to be young ($<$30 Myr). Our targets were originally taken from papers on individual disks observed with ALMA and disks that showed evidence of gaps from their SEDs. However, following the publication of the ALMA survey of the Taurus molecular cloud (Long et al. 2018), and the DSHARP survey (Andrews et al. 2018), we mostly selected targets that were from one of these two surveys because their high-resolution observations allowed for more precise estimates of gap locations in the disks and expected masses of planets that could be opening those gaps (see Table A1 for more information).

2.2. Observing Strategy

Observations started in observing semester 2015B and continued over the next 10 observing semesters (see Table A2 for more details). We observed a total of 43 protoplanetary

disk targets, with some observed multiple times for follow-up observations or to account for nonideal observing conditions.

Observations were done using two different wavefront sensors (WFSs). The observations done prior to 2019B (2019 August 1) were done primarily with the visible Shack–Hartmann WFS on the Keck II telescope. The AO correction for this WFS is operated in the R band, meaning that early in our survey we were limited to targets with bright R-band magnitudes. For the post-2019B targets in our survey, we used the Keck II infrared pyramid WFS, which performs wavefront sensing in the H band, meaning that we could observe redder targets with a better AO correction (Bond et al. 2020). We observed targets down to $H = 11.9$ and $R = 14.39$. Some targets were first observed using the Shack–Hartmann WFS and subsequently observed with the infrared pyramid WFS in order to achieve a better AO correction.

Our targets were observed with the Keck/NIRC2 vortex coronagraph using QACITS, a real-time point-spread function (PSF) centering algorithm that keeps the target star well centered on the vortex mask and stabilized during the entirety of the observing sequence (Huby et al. 2017). The vortex coronagraph allows for high-contrast imaging at small angular separations (down to ~100 mas) in the K, L', and M bands (see Xuan et al. 2018 for a performance characterization of the vortex coronagraph).

A combination of using the vortex coronagraph and multiple observing techniques (angular differential imaging (ADI) and reference star differential imaging (RDI)) allows for the most advantageous scenario for the detection of exoplanets close to their host stars. ADI and RDI are largely complementary observing strategies enabling the detection of point sources close to the central star and the characterization of any extended structure in the image.

The ADI strategy (Liu 2004; Marois et al. 2006) takes advantage of the field rotation of the sky as seen by alt-azimuth telescopes, causing any circumstellar sources (planet or disk) to rotate with time on the detector and any nonastrophysical signals due to optical effects (such as diffraction and high-order wavefront errors) to stay mostly static in time. After subtracting most quasi-static speckles using the sequence of frames, the astrophysical sources should remain, allowing for possible detection of disk structures or point sources that would otherwise be embedded in the diffracted starlight from the host star. ADI is most sensitive to point sources at regions a few diffracted beam widths (λ/D, where λ is the wavelength and D is the telescope diameter) from the star.

The RDI observing strategy uses the PSF of similar stars (in terms of stellar type and airmass at the time of observation) to characterize and remove any remaining stellar contribution (which was not suppressed by the coronagraph). See Ruane et al. (2019) for a full discussion of the benefits of utilizing RDI in the context of observing with the vortex coronagraph on Keck/NIRC2. RDI is most sensitive to areas at smaller angular separations ($\lesssim 0\farcs3$) in the frame, making it beneficial to use both observing strategies (Ruane et al. 2017). We utilize two methods of RDI, targeted RDI and single-night RDI. While we observed all of our targets in the L' band at least using ADI, for a subset of the targets we also obtained specifically targeted reference stars for RDI. These targeted RDI observations consisted of observing our science target symmetrically around transit (minimum airmass) and then observing a specifically chosen reference star (to be as similar in magnitude and airmass

as possible) for the same amount of time also centered at its transit. We chose reference stars to best represent the PSFs of our science targets but without known planets, stellar companions, or disk material. When possible, we observed each reference star centered on its time of transit for enough time so that the total number of frames and integration time were similar to those of the science target. Our reference stars were selected to match the AO performance between the reference and science targets. Therefore, we matched the H-band magnitudes when using the infrared pyramid WFS and R-band magnitudes when using the Shack–Hartmann WFS.

In addition to the use of specifically targeted reference stars, we also utilized RDI within an observing night when multiple targets were observed at L' within a night. Despite the stellar PSFs not being manually matched to those of the science targets, in the absence of specifically selected reference stars, this form of single-night RDI gives us a preliminary analysis that often achieves better contrast at smaller separations ($\lesssim 0\farcs3$) than ADI. A more refined RDI analysis with optimized reference frames taken from the library of L' vortex observations might allow for deeper achieved contrasts.

Regardless of the observing strategy, we corrected the frames for bad pixels, flat-fielded them, subtracted the sky background, registered them, and applied principal component analysis (PCA). PCA was utilized in order to estimate the stellar contribution in the images via the Vortex Image Processing (VIP) package[32] (Gomez Gonzalez et al. 2017) and the pyKLIP package[33] (Wang et al. 2015).

3. Results

3.1. Survey Sensitivity Estimates

We first compute the 5σ contrast curves for each of our targets using VIP (Figure 1). These contrast curves are computed in the same manner as described in Xuan et al. (2018). In brief, for each observation, we determine the optimal contrast curve among our different combinations of inner and outer mask sizes, reduction method (ADI and RDI), and numbers of principal components by determining the optimal contrast in any of the different combinations of those parameters in steps of 1 pixel. We do this by first generating a 5σ contrast curve for each combination of mask and frame size, number of principal components, and reduction method using VIP (Gomez Gonzalez et al. 2017) and accounting for the effects of small sample statistics as described in Mawet et al. (2014). When accounting for the small sample statistics, we fix the false-positive fraction to 2.867×10^{-7}, which is equivalent to using 5σ in the Gaussian case. We call the contrast curve generated using this assumption our 5σ contrast. VIP utilizes the fake companion method of determining the throughput (Gomez Gonzalez et al. 2017). This method involves the injection and recovery of a series of fake companions into the images in order to determine the contrast limits. We generate a 5σ contrast curve for each combination of inner and outer mask size, reduction method, and number of principal components and then compare the contrast at each 1 pixel step obtained for all versions of the contrast and take the minimum contrast achieved. We repeat this process for each
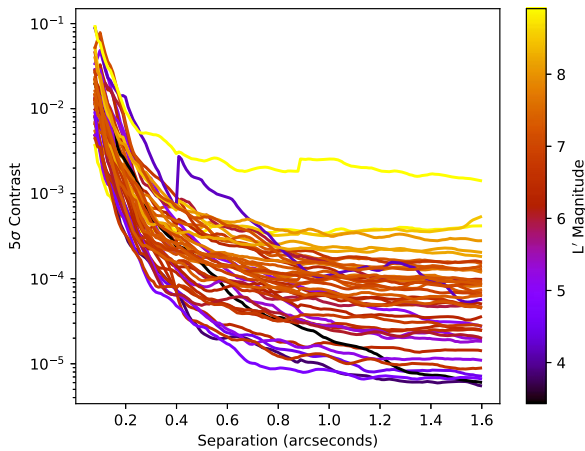
Figure 1. Optimal contrast curves for our sample of protoplanetary disks colored by the L' magnitude. Each line is the most optimal 5σ contrast for a different disk. The contrast curves at select separations are shown in Table B1 in the Appendix.

(The data used to create this figure are available.)

1 pixel step until we have an optimal contrast curve across all radial separations, which in reality represents multiple post-processing frame configurations. In the case that we have multiple data sets of the same object, we only consider the contrast curve corresponding to the more sensitive contrast in subsequent analyses (and present the optimal contrast curve for each system in Figure 1 and the corresponding contrast curves at select separations in Table B1).

For our study, we focus primarily on our `VIP` reductions, but we also compute the corresponding contrast curves using the `pyKLIP` package. After image preprocessing and registration, each image is high-pass filtered using a Gaussian kernel with a width equal to twice the FWHM of the off-axis (when the star is not on the vortex coronagraph) PSF. We then run `pyKLIP` in ADI mode with the following parameters: an exclusion parameter of half the FWHM, a maximum of 30 Karhunen–Loève modes, an inner working angle equal to twice the FWHM, an annuli width equal to about half the FWHM, and a number of reference frames limited to a maximum of the 200 most correlated images for each science frame (see Ruffio et al. 2017, for a more detailed description of the algorithm). After speckle subtraction, the images of a data set are coadded, and a Gaussian-matched filter is used as described in Ruffio et al. (2017). The width of the Gaussian kernel is equal to the PSF FWHM. The algorithm throughput is calculated from the injection and recovery of 160 simulated planets. Contrast curves are computed by taking the standard deviation of concentric annuli of the throughput-corrected match filtered images taking into account small sample statistics. Despite high-pass filtering the `pyKLIP` reductions and not high-pass filtering the `VIP` reductions, the contrasts that are achieved by the two reductions are comparable (Figure 2). We utilize both sets of reductions in order to thoroughly vet detected point sources. For `pyKLIP`, we primarily focus on the aforementioned ADI reductions. However, with `VIP`, we utilize a combination of ADI and RDI, because RDI outperformed the ADI at small separations using `VIP`, which likely helps to account for the better contrast limits for the `VIP` reductions at small separations. Additionally, the use of observation-specific

optimizations using `VIP` could also explain the improved performance of the `VIP` reductions.

3.2. Point-source Detection

In order to determine if we detect any significant point sources in our images, we generate a signal-to-noise ratio (S/N) map for each different combination of frame sizes, number of principal components, and reduction methods that were determined to be the optimal combination at each 1 pixel step in separation utilizing the `VIP` package and doing a correction to account for the effects of small sample statistics according to Mawet et al. (2014). We then create an optimal S/N map representative of our composite optimal contrast curve by taking the S/N map corresponding to the frame size, number of principal components, and reduction method that best optimizes the contrast in each 1 pixel step and making a composite S/N map consisting of each of the respective 1 pixel annuli. Since we are interested in the region of the disks where structure is seen in the millimeter, we focus on the region between $0\rlap{.}''15$ and $1\rlap{.}''6$.

Direct imaging data are plagued by stellar residuals due to imperfect removal of the stellar PSFs. Some of these residual speckles can mimic the appearance of point sources in our data. Without the use of multiwavelength data of these speckles in order to ascertain whether they have spectra similar to that of the host star, these speckles can be mistaken for astrophysical point sources. However, many of these speckles are post-processing specific, and different reduction pipelines can generate artifacts in different locations and at different S/Ns.

We determine if there are any physical point sources detected in any of our observations by first generating a list of all point sources outside of our central $0\rlap{.}''15$ mask and inside $1\rlap{.}''6$ with $S/N > 5$, utilizing the S/N maps generated from the `VIP` reductions (the locations of which are shown in Figure C1). We achieve slightly better contrast limits using the `VIP` reductions (Figure 2), so we search for point sources in that set of reductions. We exclude the known binary of AS 205 from our list of detected point sources in order to search for previously unknown companions. While we also do clearly detect PDS 70b in our observations, we do not discuss the planet nor its disk (other than showing the accompanying scattered light disk in the context of its millimeter continuum in Section 3.3), as we have thoroughly characterized the planet and its disk using the data presented herein in Wang et al. (2020).

In order to determine whether the detected point sources are real astrophysical signals instead of residual diffracted starlight, we compare the contrasts of the point sources detected with the `VIP` reductions to those of the contrasts at the same locations in the observations analyzed using `pyKLIP` (Figure 3). If these point sources were real, the fluxes measured between the two reductions should be consistent. The S/N maps using `pyKLIP` are derived from computing the standard deviation in 2 pixel wide concentric annuli. For each of the 30 point sources with $S/N > 5$ in the `VIP` S/N maps, we determine the flux and uncertainty of that point source using the maximum likelihood estimation method of the negative fake companion technique implemented in `VIP` for both our `VIP` and `pyKLIP` reductions.

The majority (24) of the 30 point sources detected in the `VIP` reductions do not have consistent (at the 2σ level or better) fluxes detected in the `pyKLIP` reductions and are therefore
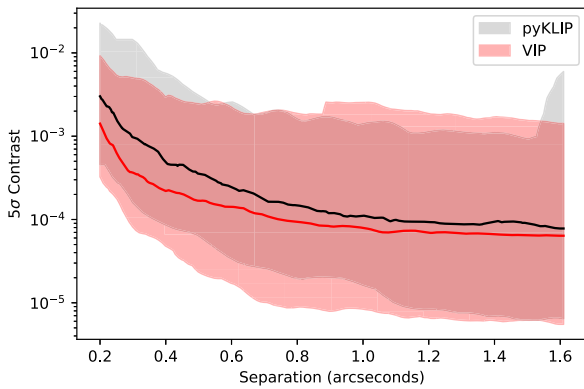
Figure 2. Comparison of the contrasts achieved using the `pyKLIP` and `VIP` reductions. The solid lines are the median contrasts of all of the contrast curves and the shaded regions represent the range of contrasts. We use ADI for the `pyKLIP` reductions and a combination of ADI and RDI for the `VIP` reductions. The improved performance of the `VIP` reductions as compared to the `pyKLIP` reductions is likely due to the additional observation-specific optimizations that were done using `VIP`. However, the contrasts are still comparable, showing the robustness of our calculated contrasts.

likely not physical. The other six point sources represent a combination of real disk detections that are consistent between the different reductions and observations where there are many residual speckles in the data sets due to imperfect speckle subtraction by both reduction algorithms. Of these six point sources, one (in HD 179218) is due to residual effects in the `VIP` RDI reductions due to poor reference star PSFs and a particularly noisy corresponding `pyKLIP` ADI reduction, two (one in CQ Tau and one in LkCa 15) are due to real disk structures that appear to be point-like but are consistent with an extended structure, two (in HL Tau) do not have the typical PSFs of point sources and instead have extended appearances likely due to diffraction from the telescope support structures, and one appears in the AS 209 data set with the poorer contrast and not in the observation with a better detection limit, indicating that it is not real. An additional way of assessing the validity of possible point sources is whether the planet-to-star contrast of a point source, as determined from the S/N maps, would have been detected given our contrast curves. While we are vetting the point sources with $S/N > 5$, this does not necessarily mean that we would be sensitive to a source of that contrast as determined from our contrast curves. Only points with contrasts above our sensitivity would have been able to be detected. Indeed, only 14 of our point sources even would have been properly detected (i.e., having contrasts above our detection sensitivity), and of these 14, none of them have consistent fluxes (at the 2σ level or better) between the two reductions.

The appearance of disk features being post-processed into apparent point sources is a well-known phenomenon (Currie et al. 2019), and indeed the presence of protoplanet(s) in LkCa 15 has been debated (e.g., Kraus & Ireland 2011; Currie et al. 2019; Follette et al. 2023). Without detailed disk modeling, it is nontrivial to disentangle disk material from a point source; therefore to err on the side of caution in the absence of such modeling (and because the flux levels of our two reductions did not agree for these points likely due to differences in post-processing), we elect to say that we do not convincingly detect planets that are coincident with the disk material in CQ Tau and LkCa 15. Therefore, by a combination of automatic and manual
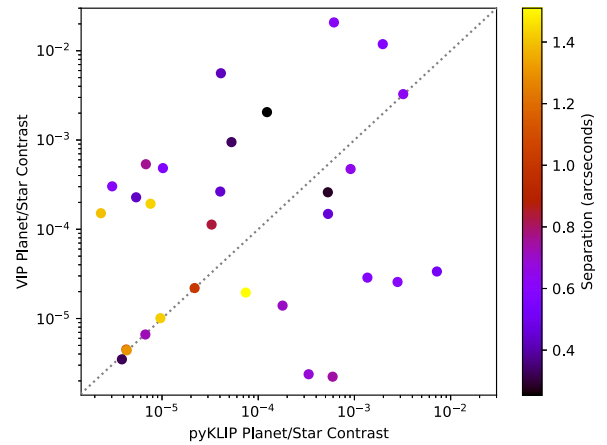
Figure 3. Comparison of the planet-to-star flux ratio of the point sources in Figure C1 determined from the `VIP` reductions vs. the planet-to-star flux ratio in the same location in the `pyKLIP` reductions. A perfectly consistent flux ratio is designated by the dotted line.

vetting, we do not convincingly detect any new point sources in our observations in the area between $0\rlap{.}''15$ and $1\rlap{.}''6$.

While we utilized both `pyKLIP` and `VIP` in order to vet potential point sources in our data, our `VIP` reductions generally achieved better contrasts than our `pyKLIP` reductions (Figure 2). Therefore, in all subsequent analyses presented herein, we present results utilizing our `VIP` reductions.

3.3. Scattered Light Disks

The direct detection of substructures in large grain dust as detected by ALMA and/or evidence of a gap or cavity in the stellar SED was a requirement of our target selection. Therefore, we might expect to see evidence of disk structure in all of our observations. However, in the case of the ALMA observed disks, the thermal emission of the millimeter/submillimeter-sized dust grains is what is being detected, whereas in the case of near-IR observations, we are sensitive to the scattered light of the micron-sized dust. Owing to viewing geometries, the scattering properties of dust grains at different wavelengths, the luminosity of the host star, data reduction techniques, and the sensitivity of our study, we would not expect to see evidence of scattered light disks in all of our targets. We do, however, see disk structures in a subset of our observations, which are consistent with the ALMA observations for these systems (Figure 4). We optimize the images shown in Figure 4 by selecting the number of principal components in our full-frame images that best show the extended structure. We reserve the direct modeling of these disks and the discussion related to the small grain dust distribution in a forthcoming study.

For purposes of our initial survey, we limit our RDI analyses to single nights (where to first order, we expect the most similar AO correction) where the stellar PSFs of any other objects observed on the same night with the vortex coronagraph at L' act as our reference library. In this initial census of detected scattered light disks, we do not optimize this reference library herein, therefore we are not detecting every disk that would be evident from a library where stellar properties are more closely matched to the science target (such as the SR 21 disk that we present in Uyama et al. 2020, where the reference PSFs are selected across different observing nights). We also do not combine multiple observing nights that might allow for the
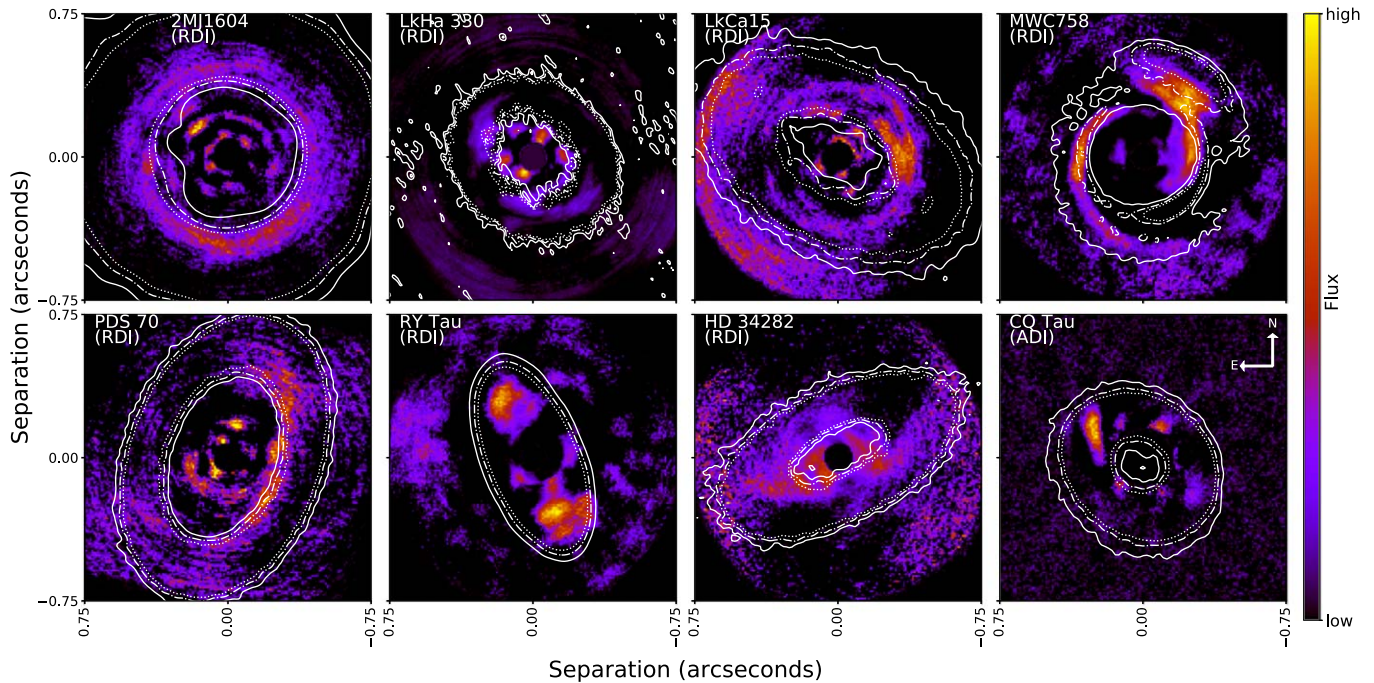
Figure 4. Disks in our survey showing evidence of structure, which is indicative of scattered light disks. We show the 1σ, 2σ, and 3σ ALMA contours (from references in Table A1) overlaid on our 3.8 μm images for reference. North is up and east is left in all of the images. We show the reduction method that optimizes the appearance of the extended structure.

increase in S/N needed to make the scattered light disk more evident (such as in the case of the HD 163296 disk presented in Guidi et al. 2018, where the disk was more visible when data over two consecutive nights were combined).

3.4. Stellar Parameters

Planet mass limits derived from observational contrast limits are a strong function of age. Therefore it is of the utmost importance that we determine accurate and self-consistently derived ages for our host stars (and therefore planetary systems). However, the ages of young stars are notoriously difficult to determine, so in order to allow for direct, population-level analyses of planet mass upper limits, we derive uniform ages for our sample of systems.

In order to estimate the stellar ages for these protoplanetary disk-hosting stars, we first attempt to compile the stellar parameters ($L_\star$, T_{eff}) required to calculate the ages of these systems as consistently as possible. Since many of the stellar parameters are sourced from references that predate updated Gaia distances (Gaia Collaboration et al. 2021), when applicable, we first rescale the stellar luminosities from the sources in Table A1 to account for the updated distances from Gaia. In the cases where uncertainties on the stellar luminosity and effective temperature are not published, we assume a 10% uncertainty in $\log(L_\star)$ and 2% uncertainty in T_{eff} (Pascucci et al. 2016).

We then estimate the stellar ages and masses using isochrones from Choi et al. (2016) in the range of 0.5–50 Myr. We interpolate the tracks to probe the mass range from 0.05–1.4 MSun, in steps of 0.01 MSun. We adopt the method described in Andrews et al. (2013) to determine stellar masses and ages. We first evaluate a likelihood function for each set of luminosities and effective temperatures (Equation (1) in Andrews et al. 2013). We then marginalize the likelihood distribution and take the median of the marginalized distribution

to estimate the age and mass of the star. We estimate the uncertainties as the 16% and 84% percentiles of these marginalized distributions (which takes into account the uncertainties on the stellar luminosity and effective temperature).

Our calculated ages are generally consistent at the 1σ level with those presented in the references in Table A1, with variations in the ages mostly due to updates to the distances to these stars as determined from updated parallaxes from Gaia (Gaia Collaboration et al. 2021). Therefore, we adopt our calculated ages in subsequent analyses. We modify our procedure for the close binary V4046 Sgr. While our derived age for this system is in agreement with a portion of the published literature, it is not in agreement with the age of the β Pictoris moving group for which it is a member. Our calculated age from our isochrone fit is $5.62^{+4.38}_{-2.46}$ Myr and the age of the β Pictoris moving group is 23 ± 3 Myr (Mamajek & Bell 2014). Notably, our calculated mass of $0.90^{+0.09}_{-0.13}$ $M_\odot$ is in good agreement with the dynamical mass of 0.90 ± 0.05 $M_\odot$ from Rosenfeld et al. (2012). Older system ages result in higher mass estimates; therefore, to be most conservative, we adopt the older age of the moving group in case the luminosity measurement was contaminated from the binary component, which was noted as a possibility in McCarthy & White (2012). Moreover, owing to the fact that all methods of estimating the ages of young stars (both the method that we employ and the methods employed in the literature for these systems) are rife with assumptions that bias the resulting ages, we also present the analysis in Sections 3.6 and 4.1 independent of system age in Appendix D to show the effect of age estimation on our mass limits.

3.5. Determining Stellar L' Magnitudes

In the absence of detecting any previously unknown point sources, we seek to place constraints on the upper limits of the masses of planets that could be creating the substructures seen at other wavelengths in these disks. We can utilize our contrast
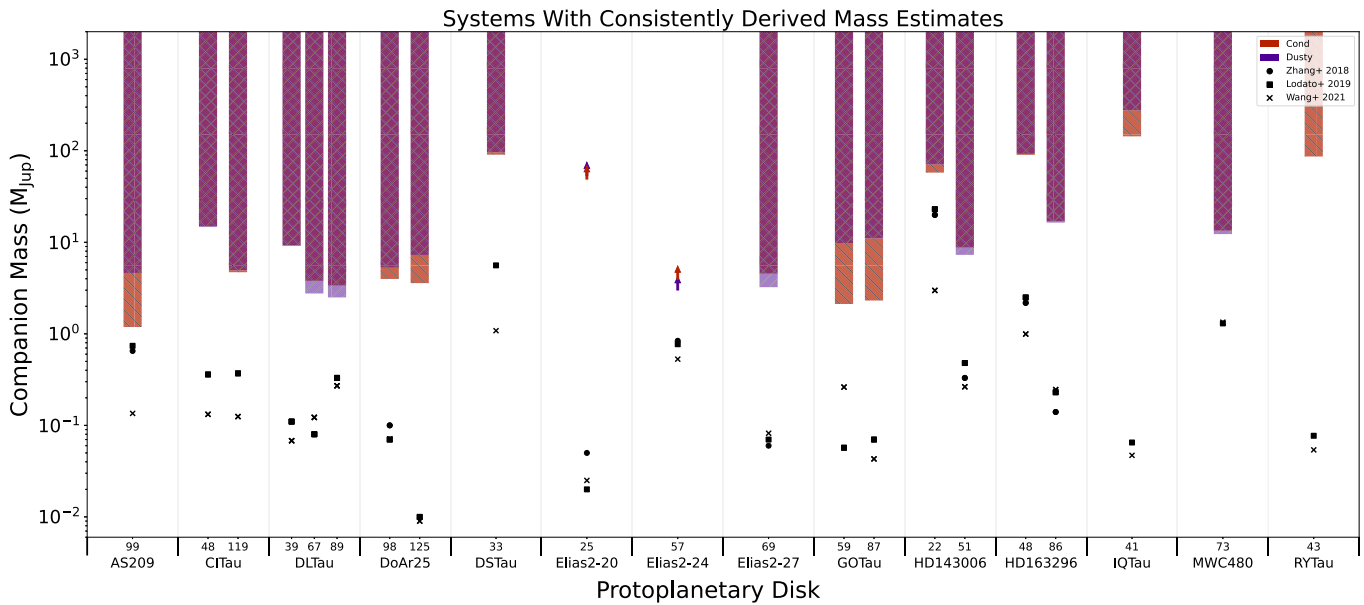
Figure 5. We show a comparison of the mass estimates from the ALMA data and our observational mass limits for the subset of our systems observed as part of the DSHARP survey (Andrews et al. 2018) or the survey of the Taurus molecular cloud (Long et al. 2018). We show the ALMA-derived planet masses (in M_{Jup}) as the points and the mass estimates derived using the AMES-Cond models from our 5σ contrast limits as the orange bars for each observed gap from the ALMA data (specified in astronomical units as the numbers above each system designation). The bars therefore represent the range of masses that we would have been sensitive to given our observations. The ages of Elias 2–20 and Elias 2–24 are lower than the youngest age in the AMES-Cond grid (1 Myr). Therefore, we show the masses assuming 1 Myr as upper limits to the ages, as younger systems would result in smaller masses. We also show the associated masses assuming the AMES-Dusty models when the masses were within the grid in purple.

limits in each of the gaps and cavities indicated by longer wavelength observations. Owing to our observing wavelength, we are more sensitive than millimeter observations to directly detecting the thermal emission of these proposed planets, and therefore our observations, despite being nondetections, can be useful in constraining the properties of these planets.

Our contrast curves can be used to estimate our mass sensitivity when paired with a host star magnitude and an evolutionary model that predicts the expected planet mass from its magnitude. In order to estimate the stellar magnitude, we utilize the WISE (for systems with W1 < 4.5) and CATWISE (for systems with W1 > 4.5) W1 and W2 measurements for each of our systems (3.4 and 4.6 μm; Marocco et al. 2021), and determine a predicted L' magnitude in order to determine the sensitivity of our observations. This is necessary as the WISE W1 and W2 bandpasses only cover a portion of the L' bandpass. Following Keppler et al. (2018), we estimate the corresponding L' magnitude by interpolating logarithmically between the W1 and W2 bands. This is necessary because these protoplanetary disk-hosting stars show strong infrared excesses and therefore are often redder than would be expected for a bare stellar photosphere.

3.6. Planetary Mass Upper Limits

In order to determine the planetary masses corresponding to our contrast constraints, we use the AMES-Cond and AMES-Dusty models (Baraffe et al. 2003; Allard et al. 2012). The AMES-Cond and AMES-Dusty models provide the expected magnitude of a planet given its mass and age. We use these grids (interpolating between the grid points), the absolute magnitude limits from our 5σ contrast curves, and the estimated stellar ages to calculate the upper limits on the planet masses. An additional important caveat to our derived mass limits is that they are estimated given the model assumptions inherent in the AMES-Cond and AMES-Dusty models (Cugno et al. 2023). We show

results using both sets of models to indicate a range of possible masses given two different model assumptions, and therefore a first-order indication of the sensitivity of our mass estimates on the chosen model.

Another important caveat for our derived masses is that we are not accounting for the effects of extinction from the circumstellar disk material. The circumstellar disk can extinct the light from a companion, meaning that our mass sensitivities may be overestimated. Indeed, when Cugno et al. (2023) accounted for the effects of 1.0 mag of extinction, the sensitivity of their survey did decrease. However, the effects of that level of extinction decreased their sensitivity by less than a factor of 2, and the uncertainties on system ages and evolutionary models can affect the derived mass estimates by an even larger factor. Determining the magnitude of the extinction for each system is also a nontrivial task and comes with additional inherent uncertainties. Therefore, while an important caveat to consider in our derived masses, we do not take extinction into account when presenting our mass limits.

High-resolution submillimeter observations of disks with substructures allow us to constrain the locations of possible gap-carving planets and can provide information about the masses of those possible planets. Zhang et al. (2018) carried out a series of 2D hydrodynamical simulations to infer the relationship between gaps in disks imaged with ALMA as part of the DSHARP survey (Andrews et al. 2018) and planet mass. This leads to direct predictions of planet masses for the objects that could be clearing out the gaps in the millimeter observations of these systems. Wang et al. (2021) utilized ALMA disk morphology and estimated the masses of planetary substructure drivers using the pebble isolation mass for a sample of systems that included the DSHARP (Andrews et al. 2018) sample and the systems imaged in Long et al. (2018). Lodato et al. (2019) also estimated the masses of planets in systems imaged as part of the DSHARP survey (Andrews et al.
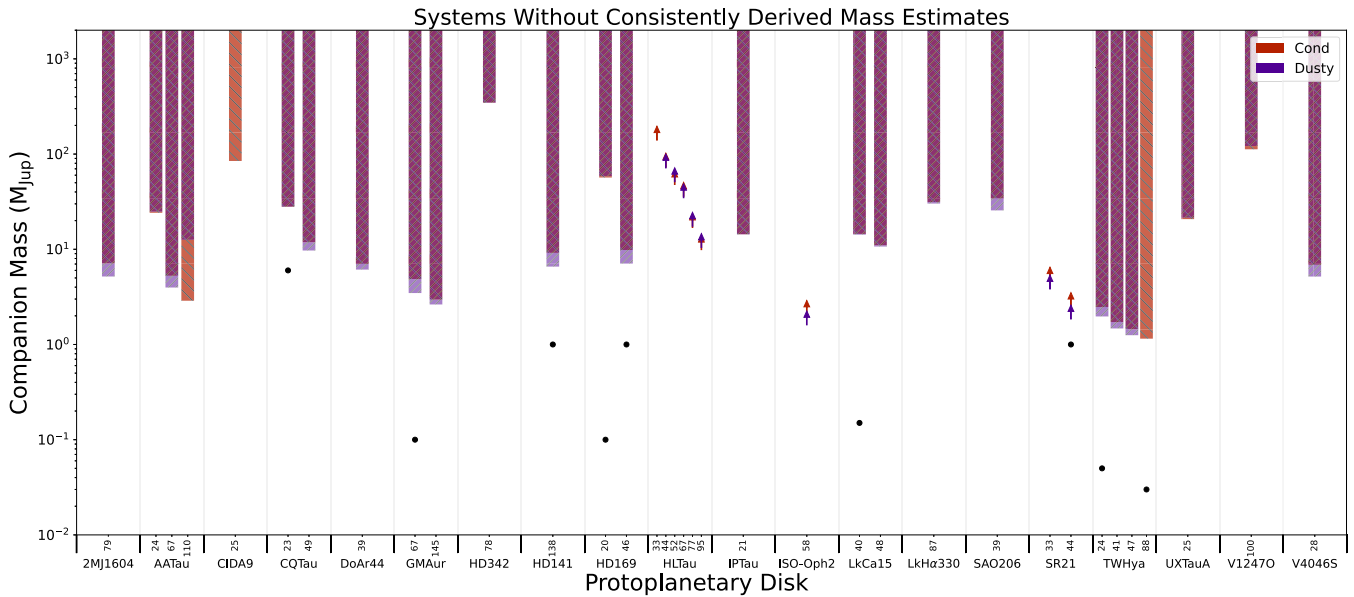
Figure 6. We show the mass estimates derived from our 5σ contrast limits (in M_{Jup}) in each gap/cavity (specified in astronomical units above each system designation) as the bars colored by radial distance from the host star. The bars therefore represent the range of masses that we would have been sensitive to given our observations. The ages for HL Tau, ISO-Oph 2, and SR 21 are lower than the youngest age in the AMES-Cond grid (1 Myr), therefore we show the masses assuming an age of 1 Myr as an upper limit to the ages, as a younger system would correspond to smaller mass. We also show the associated masses assuming the AMES-Dusty models when the masses were within the grid in purple. There is a subset of systems that have estimates of planetary masses not ascertained via the Lodato et al. (2019), Wang et al. (2021), and Zhang et al. (2018) methods. The putative companion in CQ Tau is detailed in Wölfer et al. (2021), the putative companion in GM Aur is detailed in Huang et al. (2020), and the putative companion in HD 141569 is detailed in Konishi et al. (2016). The putative companion in each of the two gaps in HD 169142 have mass estimates of between 0.1 and 1 M_{Jup} for the inner planet and 1–10M_{Jup} for the outer planet, so we show the lower limits for these masses (Fedele et al. 2017). The putative companion in SR 21 is detailed in Muro-Arena et al. (2020). The putative companions in TW Hya and LkCa 15 are detailed in Dong & Fung (2017). Additional details on NIRC2 observations of TW Hya with the vortex coronagraph can be found in Ruane et al. (2017). We show the expected planet masses as points. For the locations of the central cavities, we generally use the inner edges of the dust rings.

2018) and systems in Long et al. (2018) using empirical scaling relationships. These different methods of estimating gap-opening planet masses result in differences in the masses of these objects, which can all be compared against our companion mass upper limits.

For systems from Long et al. (2018) or Andrews et al. (2018), Figure 5 compares our mass limits, as computed from our observed 5σ contrast limits at the radial location of the planet estimated from the ALMA radial profiles, to the masses predicted in Lodato et al. (2019); Wang et al. (2021), and Zhang et al. (2018). We account for projection effects using published inclinations in each of the references cited in Table A1 and account for the new parallaxes from Gaia (Gaia Collaboration et al. 2021) to adjust the radial separations when necessary. When systems are inclined, planetary orbits trace out ellipses, resulting in changing angular separations from the host star with inclination. In order to be the most conservative in our mass limits, we take the smallest angular separation consistent with the inclination. Overall, our current mass limits are not sensitive enough to probe down to the expected masses of the planets derived from the ALMA data, consistent with the lack of new point-source detections herein.

Many of our other observed systems have detected gaps in the millimeter continuum images but are not of high enough quality to be able to use the aforementioned methods from Lodato et al. (2019), Wang et al. (2021), and Zhang et al. (2018) to ascertain the planet mass. Some of these systems also show a large inner cavity devoid of dust at longer wavelengths. Mass estimation methods from the ALMA data require a gap surrounded by dust, meaning that we cannot simply estimate the mass of a planet that could be carving out an inner cavity. This inner cavity could also
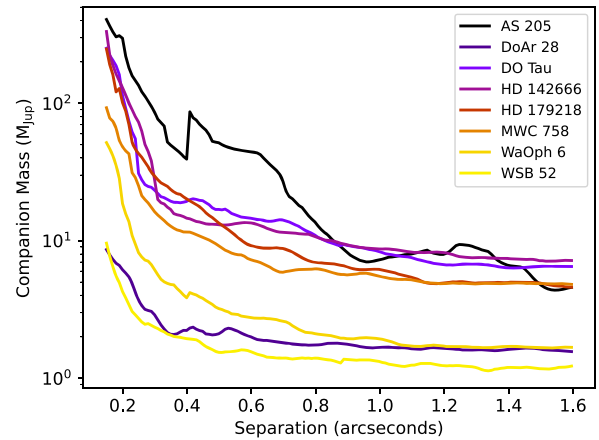
Figure 7. Companion mass upper limits (computed using the AMES-Cond model grid) as a function of the separation for the systems studied herein which did not have clear locations where a planet would be present or the locations of a gap or cavity were outside of our separation range. When the age of the system is lower than the youngest age in the AMES-Cond grid, we assume an upper limit of 1 Myr.

be due to the accretion of disk material onto the host star, making decoupling the influence of the possible planet on the disk in that inner region difficult. What is more, it is possible that the planets could visually (but not physically) co-locate with the scattered light from small dust grains outside of large cavities in our observations, making disk modeling a likely necessity to disentangle the two physical signals (e.g., PDS 70c in Wang et al. 2020; also see Quiroz et al. 2022 for more details about the benefits of utilizing disk modeling for increased sensitivity to planets). Additionally, bright disk signals at similar radii to
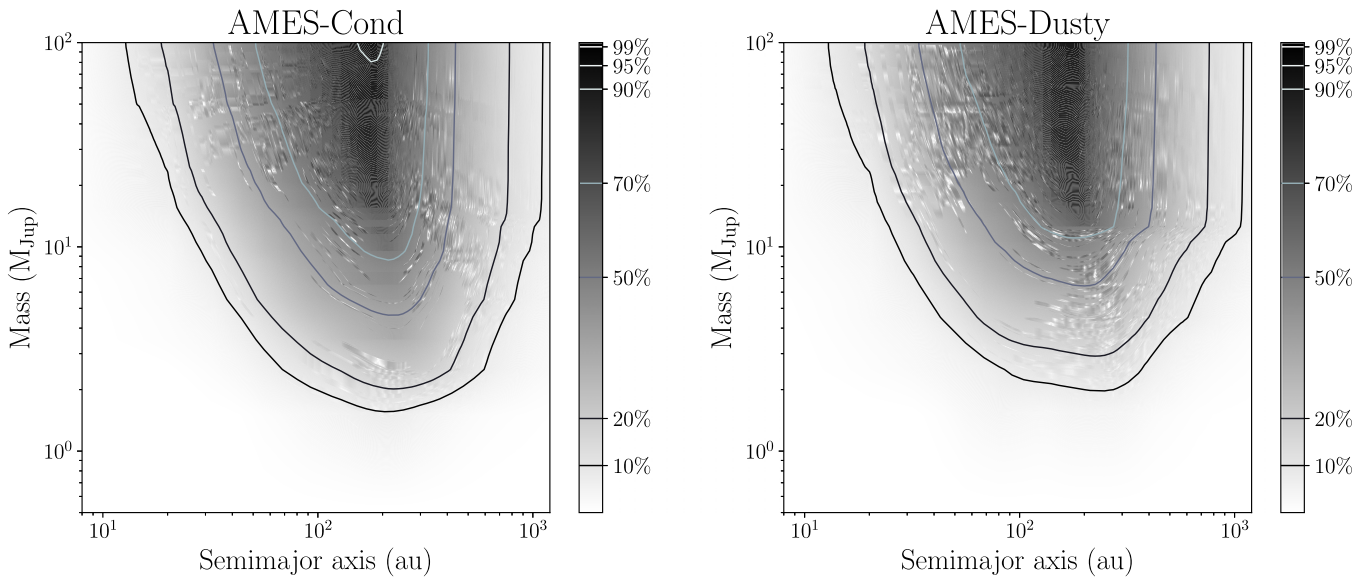
Figure 8. A map of the average sensitivity of our survey in planet mass (calculated using the AMES-Cond and AMES-Dusty models) vs. separation in astronomical units calculated using Exo-DMC (Bonavita 2020).

planets may bias both contrast curve and S/N estimates of point-like sources, and due to the filtering of extended signals into point-like sources, the use of dedicated techniques (e.g., MAYONNAISE Pairet et al. 2021, REXPACO Flasseur et al. 2021) may be necessary to reliably image both point sources and extended signals. However, there are a number of other methods to estimate the masses of planets that could be creating the cavities and gaps seen in the millimeter. We show the estimated masses of the putative companions, where available in the published literature, in Figure 6.

The other systems in our survey do not have high enough resolution ALMA data (DoAr 28 and DO Tau), did not have clear evidence for a gap in millimeter images or exact gap locations were not determined but were taken as part of the DSHARP survey (Andrews et al. 2018; WSB 52 and AS 205), are spiral systems without a consistent radial distance for which a gap is cleared (WaOph 6 and MWC 758), or have gaps/cavities outside of the distances probed by our observations (HD 142666 and HD 179218). Therefore, instead of comparing our mass detection limits to locations of interest in each disk, we calculate our mass limits over all radial separations from the host star (Figure 7). Additionally, we show our average survey sensitivity over all separations in Figure 8 determined using Exo-DMC (Bonavita 2020). In brief, Exo-DMC uses a Monte Carlo approach to determine the fraction of planets on Keplerian orbits that would have been recovered given an observational mass limit with separation. We account for the published inclinations for each of our disk systems when calculating the separations and use the default underlying eccentricity distribution from Exo-DMC.

4. Discussion

### 4.1. Investigating Disk Viscosity Constraints

Determining the mass of a planet carving out a gap at submillimeter wavelengths requires assumptions about the natal disk's viscosity, α (Zhang et al. 2018; Wang et al. 2021). Therefore, if we compare the calculated masses of planets using different values for the disk viscosity, and find that our sensitivity at L' predicts a mass that is below one or more of the masses calculated using different disk viscosities, we may be

able to place observational constraints on this parameter with the caveat that we are assuming the AMES-Cond and AMES-Dusty models. In order to compare our mass limits with those of masses determined with different values for α, we again utilize the subset of our observations with ALMA data taken as part of the DSHARP survey (Andrews et al. 2018) or the survey of systems in the Taurus molecular cloud (Long et al. 2018). The DSHARP survey is one of the highest angular resolution surveys at millimeter wavelengths, which allows for robust planetary mass predictions. Moreover, Zhang et al. (2018) directly computed the predicted masses of substructure drivers for different values of α. Wang et al. (2021) also directly computed the predicted masses of substructure-driving planets at different values of α for systems in Long et al. (2018) and Andrews et al. (2018).

As shown in Figure 9, our L' mass sensitivities do overlap with the masses predicted by the method in Zhang et al. (2018) for a number of targets when assuming $\alpha = 10^{-2}$. These overlapping values within their errors means that we cannot conclusively exclude this $\alpha = 10^{-2}$ value observationally, but it does indicate that we would possibly be sensitive to massive planets in AS 209, Elias 2-24 (the actual limit on the mass is smaller than the limit indicated by the arrow since the age of the system is younger than the lowest age in the model grids), and HD 143006. As with the mass estimations, uncertainties in the ages estimated for the host stars also add uncertainty to conclusions that can be made about the disk viscosity (see Figure D3 for a comparison of the masses derived from our 5σ contrast limits at different system ages with the masses estimated using different disk viscosities). The fact that we do not detect planets in any of these systems, might be tentative evidence that the disk viscosity for these systems (and indeed protoplanetary disks in general), might be less than this 10^{-2} value. This is consistent with α constraints from millimeter CO measurements (for example, Flaherty et al. 2018 constrained the disk viscosity to $\alpha < 0.007$ within a narrow region around the midplane of TW Hya and Villenave et al. 2022 found that $\alpha \lesssim 10^{-5}$ at 100 au in Oph 163131). However, an important caveat to this is that we are generally not sensitive enough to
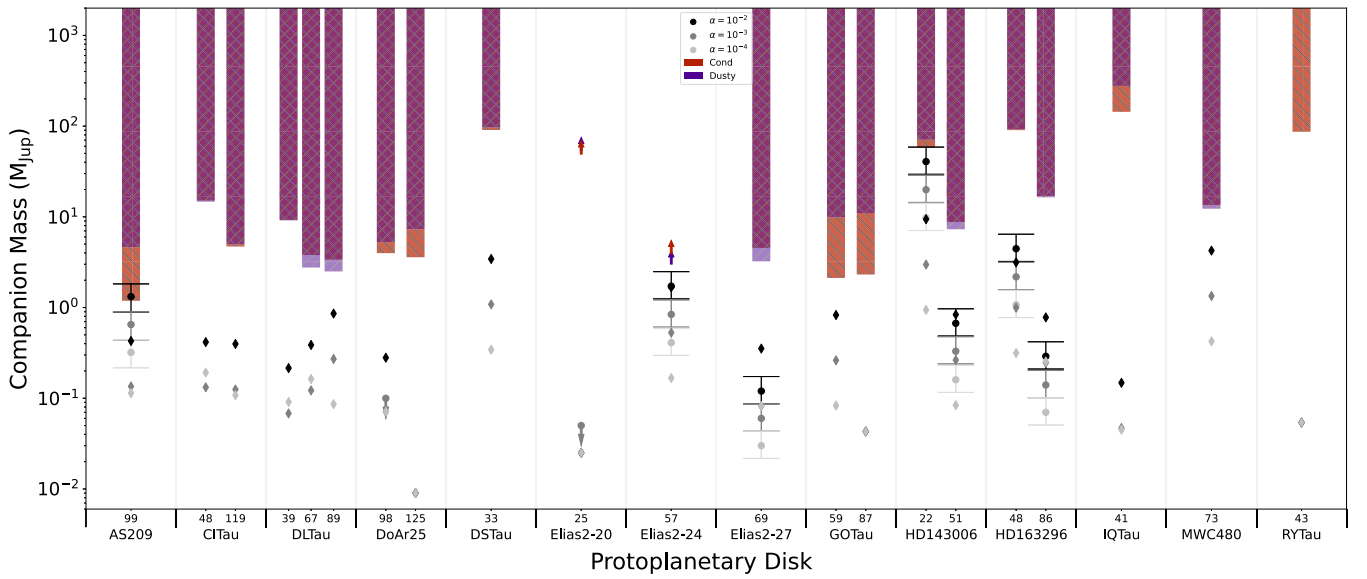
Figure 9. Expected planet masses from Wang et al. (2021; diamonds with no associated errors as none were reported) and Zhang et al. (2018; circles with their associated errors), using different values for the disk viscosity, α, are shown as black and gray points. We show our planet mass detection limits for comparison using the AMES-Cond models and AMES-Dusty models (when the masses were within the AMES-Dusty grid) for the subset of our systems observed as part of the DSHARP survey (Andrews et al. 2018) or the survey of the Taurus molecular cloud (Long et al. 2018). The bars therefore represent the range of masses that we would have been sensitive to given our observations. The ages of Elias 2–20 and Elias 2–24 are lower than the youngest age in the grids (1 Myr). Therefore, we show the masses assuming 1 Myr as upper limits to the ages, as younger systems would result in smaller masses.
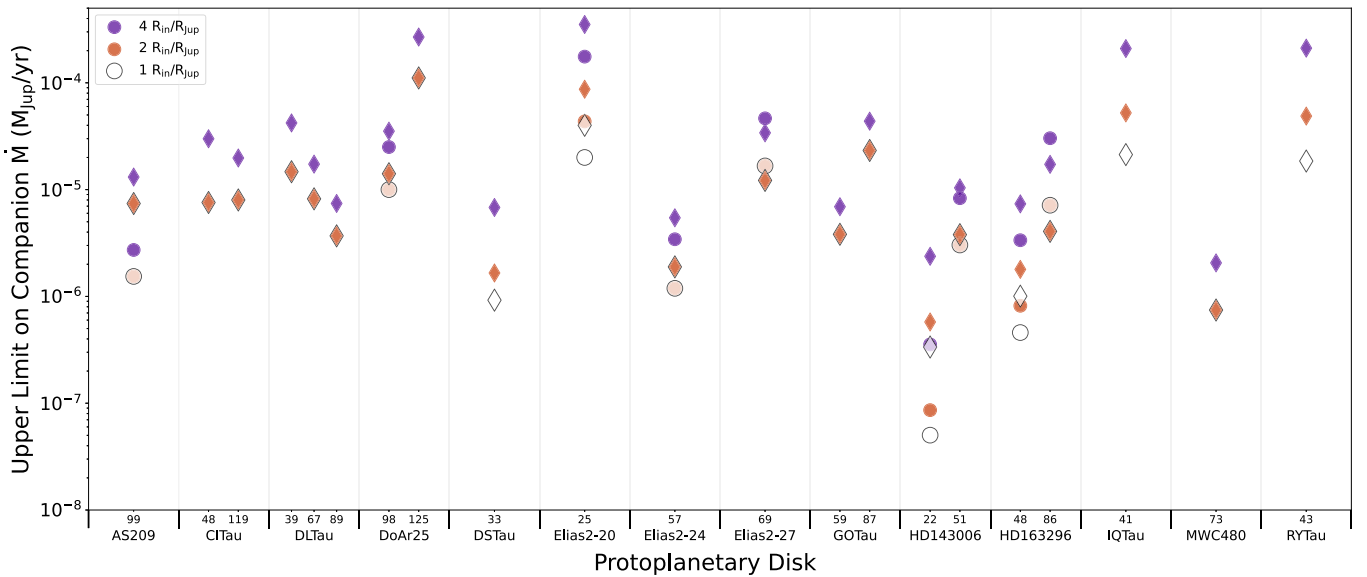
Figure 10. Upper limits on the mass accretion rates as a function of circumplanetary disk radius, R_{in}, for the subset of our systems observed as part of the DSHARP survey (Andrews et al. 2018) or the survey of the Taurus molecular cloud (Long et al. 2018), derived from Zhu (2015) and determined from our contrast limits and masses from Wang et al. (2021; diamonds) and Zhang et al. (2018; circles) assuming a disk viscosity of $\alpha = 10^{-3}$.

detect planets regardless of the disk viscosity assumed using the mass estimates from Wang et al. (2021).

4.2. Limits on Planetary Accretion Rates

Although we do not detect any new planets, and indeed do not seem to be able to achieve the sensitivity needed to directly detect the thermal emission of the planets thought to be creating the substructures seen at millimeter wavelengths (Figure 5), we can still place observational constraints on the nature of these planets. As forming protoplanets accrete their envelopes from their natal disks, the brightness associated with this accretion

can surpass the intrinsic luminosity of the planet's residual heat of formation (Zhu 2015; Szulágyi et al. 2019). Therefore, assuming that we are not sensitive enough to detect the planet's thermal emission, we can utilize our contrast limits to place constraints on the accretion, assuming all of the luminosity that would be visible would be due to accretion. Zhu (2015) related the expected magnitude to the circumplanetary accretion rate $M_p \dot{M}$. Generally, the mass of the planet cannot be disentangled from the mass accretion rate using infrared photometry, but utilizing the mass constraints from ALMA observations, and our contrast limits, we can break this degeneracy. We show the

mass accretion rates for the planets studied herein with masses derived in Wang et al. (2021) and Zhang et al. (2018) as a function of circumplanetary disk radius, R_{in}, in Figure 10. The upper limits to the mass accretion rates that we derive are larger than those from Hα measurements of the actively accreting protoplanet PDS 70c ($10^{-8.0\pm0.4}\ M_{Jup}\ yr^{-1}$; Haffert et al. 2019; Benisty et al. 2021) but are consistent with those derived from infrared observational limits (Ruane et al. 2017).

5. Conclusions

We present new deep L' observations of 43 protoplanetary disks using the NIRC2 vortex coronagraph at Keck. We primarily selected systems that had evidence of substructures in their millimeter/submillimeter continuum images in order to ascertain if we could directly detect planets that could be forming these substructures. While we do not detect any novel point sources, we are able to utilize our detection limits to place robust upper limits on the masses of planets in these disks. We present contrast curves for these systems and utilizing newly derived stellar ages, stellar L' magnitudes, and the AMES-Cond and AMES-Dusty models (Baraffe et al. 2003; Allard et al. 2012) are able to place upper limits on the masses of planets in these systems. While we are not sensitive enough to observe planets of the masses predicted for submillimeter observations, we do probe down to $\sim 1\ M_{Jup}$ for a number of systems that we have observed. This means that if planets are the primary driver for the observed substructures in the submillimeter observations of these disks, then they must be under our observational sensitivity for each system and sub-Jovian for a number of our observed systems, given the caveat that we are not accounting for extinction and given the underlying assumptions of the AMES-Cond and AMES-Dusty models. Utilizing our mass upper limits, we also investigate constraints that we can place on the viscosity of the disk, possibly allowing us to exclude $\alpha > 10^{-2}$. From our observational sensitivities and the masses derived from ALMA observations, we are able to place limits on the mass accretion rates for a subset of systems studied herein.

We also detect scattered light disks in a number of our observations, which would allow for a detailed study of the properties of the dust in protoplanetary disks when observed at multiple wavelengths. By virtue of the fact that we purposely selected targets that have been observed at other wavelengths, many of our disks that show evidence of structure have been observed in the near-infrared by facilities such as GPI or SPHERE. However, our additional observations in a different wavelength and/or utilizing the vortex coronagraph to probe smaller separations allow for a unique perspective into these systems. Multiwavelength studies of protoplanetary disks will provide insight into the radial distributions of different-sized dust in these disks, ultimately allowing for a better understanding of the natal disk environment and the availability of planetary building blocks. We reserve extensive modeling and discussion of these disks in a forthcoming paper.

Future observations of these systems with the next generation of larger primary mirror ground-based telescopes will likely be needed in order to reach down to the sensitivities required to detect these planets directly. Achieving the sensitivity needed to observe planets of the masses predicted by millimeter observations will be needed to definitively ascertain the nature of the disk substructures revealed by ALMA.

Appendix A
System Parameters and Observing Details

We show the system parameters in Table A1 and the observation details in Table A2.

Table A1
System Parameters

System	Distance[a] (pc)	$T_{\rm eff}$ (K)	L[b] ($L_\odot$)	$M_\star$[c] ($M_\odot$)	Age[c] (Myr)	L'[d] (mag)	References[e]
2MJ1604[f]	145.31 ± 0.57	4898 ± 180	0.58 ± 0.19	1.01 ± 0.11	$15.85^{+12.33}_{-6.94}$	7.58 ± 0.02	1, 2
AA Tau	134.67 ± 1.57	3763 ± 173[g]	0.41 ± 0.10	$0.56^{+0.16}_{-0.12}$	$2.51^{+2.50}_{-1.10}$	7.19 ± 0.02	3, 4
AS 205	132.06 ± 1.25	4266 ± 295	2.28 ± 0.75	$0.88^{+0.31}_{-0.26}$	$0.79^{+1.44}_{-0.44}$	4.19 ± 0.34	5, 6
AS 209	121.25 ± 0.43	4266 ± 295	1.42 ± 0.67	$0.87^{+0.23}_{-0.22}$	$1.58^{+3.43}_{-0.95}$	6.53 ± 0.03	5, 5
CIDA 9	175.08 ± 2.69	3585 ± 165[g]	0.21 ± 0.05	$0.45^{+0.14}_{-0.10}$	$4.47^{+4.45}_{-2.23}$	8.91 ± 0.01	3, 7
CI Tau	160.32 ± 0.53	4277 ± 197[g]	0.83 ± 0.19	$0.92^{+0.14}_{-0.17}$	$2.82^{+2.19}_{-1.23}$	6.79 ± 0.02	3, 7
CQ Tau	149.37 ± 1.34	6900 ± 318	8.93 ± 2.07	$1.57^{+0.11}_{-0.10}$	$11.22^{+11.17}_{-2.31}$	6.63 ± 0.06	8, 9
DL Tau	159.94 ± 0.50	4277 ± 197[g]	0.65 ± 0.15	$0.92^{+0.12}_{-0.15}$	$3.98^{+3.10}_{-1.74}$	6.78 ± 0.02	3, 7
DoAr 25	138.16 ± 0.82	4266 ± 295	0.96 ± 0.46	$0.86^{+0.21}_{-0.20}$	$2.51^{+4.57}_{-1.39}$	7.24 ± 0.02	5, 5
DoAr 28	135.60 ± 0.49	4350 ± 200	1.28 ± 0.30	0.95 ± 0.18	$1.78^{+1.38}_{-0.78}$	8.13 ± 0.02	10, 11
DoAr 44	146.32 ± 0.49	4730 ± 218	1.92 ± 0.45	$1.26^{+0.12}_{-0.19}$	$2.00^{+1.55}_{-0.87}$	6.68 ± 0.03	12, 13
DO Tau	138.52 ± 0.68	3806 ± 175[g]	0.22 ± 0.05	$0.61^{+0.12}_{-0.13}$	$7.08^{+5.51}_{-3.10}$	5.98 ± 0.05	3, 14
DS Tau	158.35 ± 0.53	3792 ± 175[g]	0.24 ± 0.06	$0.61^{+0.12}_{-0.13}$	$6.31^{+4.91}_{-3.15}$	7.26 ± 0.02	3, 7
Elias 2-20	137.53 ± 3.96	3890 ± 269	2.22 ± 1.07	$0.58^{+0.22}_{-0.13}$	$0.63^{+4.38}_{-0.41}$	5.95 ± 0.05	5, 5
Elias 2-24	139.26 ± 1.24	4266 ± 295	6.32 ± 2.87	$0.92^{+0.36}_{-0.22}$	$0.35^{+1.23}_{-0.20}$	6.42 ± 0.03	5, 5
Elias 2-27	110.07 ± 10.30	3890 ± 269	0.82 ± 0.51	$0.61^{+0.20}_{-0.18}$	$2.51^{+8.71}_{-1.80}$	7.22 ± 0.02	5, 5
GM Aur	158.11 ± 1.22	4115 ± 190[g]	0.62 ± 0.15	$0.81^{+0.14}_{-0.16}$	$3.16^{+2.46}_{-1.38}$	8.17 ± 0.01	3, 15
GO Tau	142.38 ± 0.41	3516 ± 162[g]	0.21 ± 0.05	$0.40^{+0.13}_{-0.10}$	$3.16^{+3.92}_{-1.38}$	8.84 ± 0.02	3, 7
HD 34282	308.61 ± 2.20	9250 ± 125	14.66 ± 0.67	$1.95^{+0.02}_{-0.01}$	$19.95^{+15.53}_{-7.36}$	7.04 ± 0.02	16, 17
HD 141569	111.61 ± 0.36	9750 ± 125	25.34 ± 0.58	2.20 ± 0.01	$17.78^{+17.70}_{-8.87}$	6.70 ± 0.02	16, 18
HD 142666	146.25 ± 0.46	7586 ± 350	8.91 ± 4.58	$1.62^{+0.11}_{-0.09}$	$19.95^{+15.53}_{-9.95}$	5.32 ± 0.08	5, 5
HD 143006	167.34 ± 0.51	5623 ± 259	3.91 ± 1.34	$1.68^{+0.26}_{-0.25}$	$4.47^{+4.45}_{-1.95}$	6.28 ± 0.04	5, 5
HD 163296	100.97 ± 0.42	9333 ± 645	16.97 ± 12.69	$2.05^{+0.16}_{-0.14}$	$15.85^{+15.77}_{-6.94}$	3.43 ± 0.44	5, 5
HD 169142	114.87 ± 0.35	7500 ± 346	5.90 ± 5.60	$1.58^{+0.11}_{-0.09}$	$19.95^{+15.53}_{-8.73}$	6.30 ± 0.04	19, 20
HD 179218	260.09 ± 2.23	9640 ± 444	104.85 ± 30.00	$2.52^{+0.34}_{-0.32}$	$3.55^{+14.23}_{-1.31}$	4.48 ± 0.25	21, 22
HL Tau	147.3 ± 0.5[h]	4400 ± 203	9.25 ± 5.50	$1.03^{+0.28}_{-0.20}$	$0.32^{+1.68}_{-0.17}$	5.07 ± 0.08	23, 24
IP Tau	129.38 ± 0.29	3763 ± 173[g]	0.33 ± 0.08	$0.58^{+0.14}_{-0.13}$	$3.55^{+3.53}_{-1.55}$	7.62 ± 0.01	3, 7
IQ Tau	131.51 ± 0.62	3690 ± 170[g]	0.22 ± 0.05	$0.53^{+0.14}_{-0.12}$	$5.62^{+5.60}_{-2.81}$	7.13 ± 0.02	3, 7
ISO-Oph 2	134.25 ± 7.56	3467 ± 160	0.71 ± 0.17	$0.31^{+0.09}_{-0.05}$	$0.40^{+0.40}_{-0.24}$	8.44 ± 0.02	25, 26
LkCa 15	157.19 ± 0.65	4277 ± 197[g]	0.77 ± 0.18	$0.92^{+0.14}_{-0.16}$	$3.16^{+2.46}_{-1.38}$	7.67 ± 0.02	3, 27
LkHα 330	318.22 ± 3.49	6220 ± 287[g]	16.55 ± 3.84	$2.24^{+0.32}_{-0.26}$	$3.16^{+1.85}_{-1.17}$	6.40 ± 0.04	3, 12
MWC 480	156.22 ± 1.26	8250 ± 380	17.81 ± 5.50	$1.85^{+0.12}_{-0.10}$	$14.13^{+17.50}_{-7.05}$	4.73 ± 0.09	19, 7
MWC 758	155.87 ± 0.76	8130 ± 375	16.30 ± 3.79	$1.84^{+0.11}_{-0.09}$	$12.59^{+15.59}_{-5.51}$	5.18 ± 0.10	28, 29
PDS 70	112.39 ± 0.24	3972 ± 36	0.34 ± 0.09	$0.75^{+0.03}_{-0.04}$	$5.62^{+4.38}_{-2.08}$	8.01 ± 0.02	30, 31
RY Tau	138.22 ± 3.88	5930 ± 273[g]	11.93 ± 2.77	$2.28^{+0.34}_{-0.31}$	$2.51^{+1.95}_{-1.10}$	3.82 ± 0.11	3, 7
SAO 206462	135.00 ± 0.44	6250 ± 125	5.17 ± 0.12	$1.45^{+0.04}_{-0.01}$	$10.00^{+1.22}_{-1.09}$	5.26 ± 0.09	16, 32
SR 21	136.43 ± 0.56	4571 ± 211	3.77 ± 0.88	$1.20^{+0.29}_{-0.25}$	$0.71^{+0.70}_{-0.31}$	6.04 ± 0.03	25, 33
TW Hya	60.14 ± 0.05	3776 ± 174[g]	0.24 ± 0.05	0.59 ± 0.13	$6.31^{+4.91}_{-3.15}$	7.20 ± 0.02	3, 34
UX Tau A	142.23 ± 0.67	4870 ± 224[g]	1.64 ± 0.38	$1.27^{+0.09}_{-0.13}$	$3.16^{+3.15}_{-1.38}$	6.87 ± 0.02	3, 12
V1247 Ori	401.30 ± 3.16	7250 ± 334	14.59 ± 1.50	$1.80^{+0.08}_{-0.06}$	$7.08^{+0.86}_{-0.77}$	6.42 ± 0.03	35, 36
V4046 Sgr	71.48 ± 0.11	4260 ± 196	0.49 ± 0.11	$0.90^{+0.09}_{-0.13}$	$5.62^{+4.38}_{-2.46}$, 23 ± 3[i]	7.27 ± 0.02	37, 38
WaOph 6	122.53 ± 0.35	4169 ± 288	2.86 ± 1.38	$0.78^{+0.28}_{-0.20}$	$0.71^{+2.45}_{-0.46}$	6.36 ± 0.03	5, 5
WSB 52	135.27 ± 0.92	3715 ± 257	0.70 ± 0.34	$0.51^{+0.19}_{-0.17}$	$1.78^{+7.13}_{-1.22}$	7.32 ± 0.02	5, 5

Notes.

[a] We use parallax values from Gaia EDR3 (Gaia Collaboration et al. 2021).

[b] We scale the luminosities in the cited references to the new distances from Gaia EDR3 (Gaia Collaboration et al. 2021).

[c] Our ages and stellar masses, computed using fits to isochrones (as described in Section 3.4).

[d] We calculate L' magnitudes by logarithmically interpolating the WISE W1 and W2 magnitudes. See Section 3.5 for more information.

[e] Reference for the source of the initial stellar parameters (that were rescaled when necessary to account for new distances from Gaia EDR3; Gaia Collaboration et al. 2021) and a reference for a different wavelength observation of the disk.

[f] Full name: 2MASS J16042165-2130284.

[g] The $T_{\rm eff}$ for this system is determined using Table 5 in Herczeg & Hillenbrand (2014), where we interpolate between stellar types when necessary.

[h] Parallax measurement from Galli et al. (2018).

[i] While the mass that we derive from our isochrone fit is consistent with the published dynamical mass (Rosenfeld et al. 2012) and our derived age ($5.62^{+4.38}_{-2.46}$ Myr) is consistent with a portion of the published ages for this system, the age is at odds with that of the β Pictoris moving group (23 ± 3 Myr) for which it is a member (Mamajek & Bell 2014). V4046 Sgr is a tight binary, so despite the agreement of our masses, we elect to use 23 ± 3 Myr as the age of this system to mitigate any possible contamination of the stellar luminosity from the binary component.

References. (1) Carpenter et al. (2014), (2) Zhang et al. (2014), (3) Herczeg & Hillenbrand (2014), (4) Loomis et al. (2017), (5) Andrews et al. (2018), (6) Kurtovic et al. (2018), (7) Long et al. (2018), (8) Testi et al. (2003), (9) Ubeira Gabellini et al. (2019), (10) Kim et al. (2013), (11) Rich et al. (2015), (12) Andrews et al. (2011), (13) Cieza et al. (2021), (14) Kwon et al. (2015), (15) Huang et al. (2020), (16) Guzmán-Díaz et al. (2021), (17) van der Plas et al. (2017), (18) Konishi et al. (2016), (19) Meeus et al. (2012), (20) Fedele et al. (2017), (21) Menu et al. (2015), (22) Kluska et al. (2018), (23) van der Marel et al. (2019), (24) Carrasco-González et al. (2019), (25) Manara et al. (2015), (26) González-Ruilova et al. (2020), (27) Isella et al. (2012), (28) Boehler et al. (2018), (29) Dong et al. (2018), (30) Keppler et al. (2018), (31) Keppler et al. (2019), (32) van der Marel et al. (2016), (33) Pinilla et al. (2015), (34) Nomura et al. (2016), (35) Kraus et al. (2013), (36) Kraus et al. (2017), (37) McCarthy & White (2012), (38) Rosenfeld et al. (2013).

(This table is available in machine-readable form.)

Table A2
Observation Log

System	UT Date	Total Number of Frames	Total Integration Time (s)	Parallactic Angular Rotation (°)
2MJ1604[a]	2017-05-10	73	3285.0	36.2
AA Tau	2020-10-25	153	4590.0	161.3
AS 205	2019-06-18	43	1290.0	139.4
AS 209	2018-05-26	60	2700.0	33.0
	2018-05-28	145	4350.0	54.0
	2018-07-23	90	2700.0	27.1
	2018-07-30	120	3600.0	44.5
CIDA 9	2020-10-25	83	2490.0	18.5
CI Tau	2018-10-21	132	3960.0	161.2
	2018-12-23	87	2610.0	182.0
CQ Tau	2018-12-24	60	1800.0	111.0
DL Tau	2019-01-09	160	4800.0	220.3
DoAr 25	2019-06-08	64	1920.0	30.9
DoAr 28	2017-07-01	90	4050.0	41.7
DoAr 44	2017-06-13	54	1620.0	21.4
	2017-06-30	100	3750.0	42.1
DO Tau	2020-10-09	44	1188.0	19.0
DS Tau	2020-10-09	65	1950.0	78.9
Elias 2-20	2020-05-29	143	7150.0	72.4
Elias 2-24	2019-02-17	20	600.0	8.2
	2020-06-01	161	4830.0	56.9
Elias 2-27	2019-05-22	30	900.0	16.9
	2020-05-30	131	3930.0	54.7
GM Aur	2017-01-14	120	5400.0	126.7
GO Tau	2020-11-27	90	2700.0	11.5
HD 34282	2017-02-07	73	3285.0	61.3
	2017-10-12	49	1470.0	24.6
	2017-10-13	139	4170.0	60.7
HD 141569	2015-06-11	39	780.0	49.3
HD 142666	2019-06-18	75	2250.0	38.7
HD 143006	2019-05-21	76	2280.0	42.5
	2019-06-08	60	1800.0	29.2
HD 163296	2017-05-31	80	2400.0	40.4
HD 169142	2020-05-31	78	2340.0	28.9
HD 179218	2016-08-14	45	2025.0	130.1
	2016-09-11	25	1200.0	0.4
	2016-10-17	30	1440.0	0.8
	2017-06-01	80	2400.0	131
HL Tau	2015-10-22	10	250.0	0.1
	2017-12-26	105	2100.0	161.3
IP Tau	2017-10-03	130	5460.0	211.6
IQ Tau	2020-11-27	84	2520.0	16.5
ISO-Oph 2	2021-05-19	237	7110.0	68.4
LkCa 15	2015-10-22	81	2025.0	156.9
	2015-10-24	22	550.0	8.5
	2015-12-27	50	1500.0	129.6
	2017-01-12	101	2272.5	160.8
	2020-10-10	101	3030.0	43.7
LkHα 330	2015-10-22	44	1100.0	41.1
	2018-12-25	93	2790.0	38.3
MWC 480	2018-12-23	80	2400.0	132.2
	2018-12-24	140	4200.0	87.9
MWC 758	2015-10-24	81	2025.0	128.8
	2016-10-24	80	3200.0	173.2
PDS 70	2019-06-08	42	1260.0	27.8
RY Tau	2015-10-22	33	825.0	12.0
	2015-10-24	83	2075.0	105.3
SAO 206462	2016-05-27	80	2400.0	23.0
SR 21	2020-05-31	137	4110.0	56.3
TW Hya	2016-04- 13	70	2100.0	21.6
	2017-01-09	120	5400.0	44.4
	2017-01-13	117	5265.0	44.7
	2019-02-17	64	1920.0	33.2

Table A2
(Continued)

System	UT Date	Total Number of Frames	Total Integration Time (s)	Parallactic Angular Rotation (°)
UX Tau A	2016-10-16	116	2320.0	199.5
	2017-02-11	50	1200.0	156.3
	2017-10-04	128	5376.0	164.2
V1247 Ori	2017-12-27	51	1530.0	4.0
V4046 Sgr	2017-05-11	70	3150.0	28.3
WaOph 6	2020-05-30	41	1230.0	13.3
WSB 52	2020-06-02	168	5040.0	68.3

Note.
[a] Full name: 2MASS J16042165-2130284.

Appendix B
Contrast Curves

We show the most optimal 5σ contrast curves for each target interpolated to selected separations in Table B1.

Table B1
5σ Optimal Contrasts at Select Locations

	0″15	0″2	0″4	0″6	0″8	1″0	1″2	1″4	1″6
2M J16042165-213	3.60E-03	1.91E-03	3.01E-04	1.85E-04	1.09E-04	1.05E-04	9.29E-05	1.01E-04	8.29E-05
AA Tau	2.52E-03	1.03E-03	1.93E-04	1.40E-04	1.16E-04	1.05E-04	1.04E-04	1.03E-04	9.38E-05
AS 205	1.86E-02	1.35E-02	9.33E-04	9.07E-04	2.46E-04	1.11E-04	1.26E-04	9.62E-05	5.69E-05
AS 209	1.28E-03	6.35E-04	7.82E-05	4.84E-05	3.44E-05	2.86E-05	2.56E-05	2.49E-05	2.47E-05
CIDA 9	2.35E-02	9.21E-03	2.98E-03	2.23E-03	1.88E-03	2.54E-03	1.86E-03	1.70E-03	1.42E-03
CI Tau	2.44E-03	1.08E-03	2.15E-04	1.44E-04	1.16E-04	1.03E-04	9.51E-05	9.00E-05	8.72E-05
CQ Tau	1.36E-03	4.79E-04	6.93E-05	2.07E-05	1.23E-05	1.22E-05	1.06E-05	9.89E-06	8.90E-06
DL Tau	8.32E-04	3.27E-04	7.97E-05	4.69E-05	3.18E-05	3.74E-05	3.41E-05	3.07E-05	2.80E-05
DoAr 25	4.04E-03	1.46E-03	2.62E-04	1.74E-04	1.41E-04	1.21E-04	1.07E-04	1.00E-04	8.73E-05
DoAr 28	3.89E-03	2.37E-03	4.37E-04	3.49E-04	2.56E-04	2.36E-04	2.28E-04	2.20E-04	2.05E-04
DoAr 44	3.23E-03	1.26E-03	1.51E-04	9.14E-05	5.95E-05	6.69E-05	4.91E-05	5.96E-05	4.55E-05
DO Tau	1.47E-02	6.16E-03	7.80E-04	4.02E-04	2.37E-04	1.51E-04	1.00E-04	9.09E-05	9.48E-05
DS Tau	6.42E-03	2.70E-03	4.75E-04	2.76E-04	2.19E-04	1.65E-04	1.71E-04	1.62E-04	1.50E-04
Elias 2-20	3.03E-03	6.77E-04	1.55E-04	9.55E-05	5.77E-05	5.17E-05	4.84E-05	4.73E-05	4.61E-05
Elias 2-24	3.63E-03	1.38E-03	2.75E-04	1.80E-04	8.96E-05	6.14E-05	5.77E-05	4.97E-05	4.64E-05
Elias 2-27	6.11E-03	2.22E-03	6.80E-04	2.76E-04	1.90E-04	1.58E-04	1.38E-04	1.41E-04	1.28E-04
GM Aur	3.03E-03	1.52E-03	3.43E-04	2.96E-04	2.34E-04	2.11E-04	2.21E-04	2.01E-04	1.83E-04
GO Tau	8.00E-04	4.97E-04	3.74E-04	4.12E-04	3.67E-04	3.51E-04	3.81E-04	3.75E-04	4.18E-04
HD 34282	3.63E-03	1.70E-03	3.21E-04	1.75E-04	9.72E-05	1.04E-04	8.10E-05	8.57E-05	6.86E-05
HD 141569	7.87E-03	3.38E-03	9.09E-04	3.06E-04	2.10E-04	1.77E-04	1.60E-04	1.60E-04	1.59E-04
HD 142666	4.96E-03	1.50E-03	1.30E-04	9.24E-05	4.32E-05	2.77E-05	2.44E-05	1.97E-05	1.84E-05
HD 143006	2.46E-03	9.53E-04	1.40E-04	8.01E-05	6.29E-05	4.39E-05	3.78E-05	3.52E-05	3.56E-05
HD 163296	6.07E-03	2.38E-03	2.38E-04	7.09E-05	3.49E-05	1.94E-05	1.23E-05	7.34E-06	6.06E-06
HD 169142	3.81E-03	1.20E-03	1.41E-04	9.24E-05	6.99E-05	6.28E-05	5.97E-05	5.85E-05	5.09E-05
HD 179218	1.67E-03	7.08E-04	7.35E-05	2.32E-05	1.50E-05	1.23E-05	8.20E-06	8.35E-06	7.17E-06
HL Tau	1.41E-02	4.68E-03	4.77E-04	1.61E-04	9.99E-05	7.17E-05	4.37E-05	3.20E-05	2.77E-05
IP Tau	2.25E-03	9.30E-04	2.10E-04	1.38E-04	1.15E-04	1.00E-04	1.06E-04	1.10E-04	8.56E-05
IQ Tau	2.65E-02	6.73E-03	6.95E-04	4.21E-04	1.95E-04	1.51E-04	1.33E-04	1.37E-04	1.39E-04
ISO-Oph 2	6.43E-03	3.73E-03	6.62E-04	4.43E-04	3.23E-04	3.25E-04	3.75E-04	3.58E-04	5.34E-04
LkCa 15	3.04E-03	1.49E-03	4.07E-04	1.97E-04	1.63E-04	1.46E-04	1.28E-04	1.30E-04	1.20E-04
LkHα 330	2.66E-03	1.01E-03	1.18E-04	4.97E-05	3.22E-05	2.72E-05	2.40E-05	2.71E-05	2.50E-05
MWC 480	1.04E-03	4.40E-04	4.79E-05	1.71E-05	8.85E-06	8.39E-06	7.13E-06	6.85E-06	6.66E-06
MWC 758	1.15E-03	5.76E-04	6.41E-05	2.55E-05	1.91E-05	1.47E-05	1.13E-05	1.15E-05	1.10E-05
PDS 70	6.67E-03	3.68E-03	7.36E-04	4.67E-04	3.78E-04	3.20E-04	3.07E-04	2.82E-04	2.80E-04
RY Tau	1.30E-03	3.25E-04	7.29E-05	2.04E-05	1.35E-05	8.88E-06	6.59E-06	6.13E-06	5.52E-06
SAO 206462	8.51E-03	3.80E-03	1.95E-04	1.26E-04	6.15E-05	3.20E-05	2.14E-05	2.36E-05	1.96E-05
SR 21	1.51E-03	5.02E-04	6.45E-05	5.80E-05	3.96E-05	2.52E-05	2.34E-05	2.31E-05	2.02E-05
TW Hya	2.01E-03	1.07E-03	2.50E-04	1.44E-04	7.59E-05	6.27E-05	4.96E-05	5.16E-05	4.61E-05
UX Tau A	2.44E-03	1.76E-03	2.25E-04	1.16E-04	8.59E-05	8.66E-05	8.29E-05	7.20E-05	6.35E-05

	0″15	0″2	0″4	0″6	0″8	1″0	1″2	1″4	1″6
V1247 Ori	1.23E-03	6.96E-04	7.18E-05	2.87E-05	1.82E-05	1.75E-05	1.55E-05	1.41E-05	1.43E-05
V4046 Sgr	2.99E-03	1.46E-03	2.12E-04	1.93E-04	1.05E-04	9.95E-05	7.37E-05	8.99E-05	7.40E-05
WaOph 6	1.43E-02	3.62E-03	4.40E-04	2.48E-04	1.61E-04	1.32E-04	1.02E-04	1.01E-04	9.83E-05
WSB 52	2.14E-03	6.33E-04	1.56E-04	9.66E-05	7.97E-05	7.20E-05	6.49E-05	6.20E-05	6.42E-05

Appendix C
Locations of Point-source Detections

We show the locations of the point sources that had $S/N > 5$ between 0″15 and 1″6 in our `VIP` reductions. We vet these point sources in Section 3.2 and conclude that none of them present convincing evidence that they represent astrophysical point sources. As evident by the weighted histogram in Figure C1, we have more false positives at smaller separations due to imperfect starlight suppression, and because of the higher false-positive rate for fixed S/N at smaller separations.
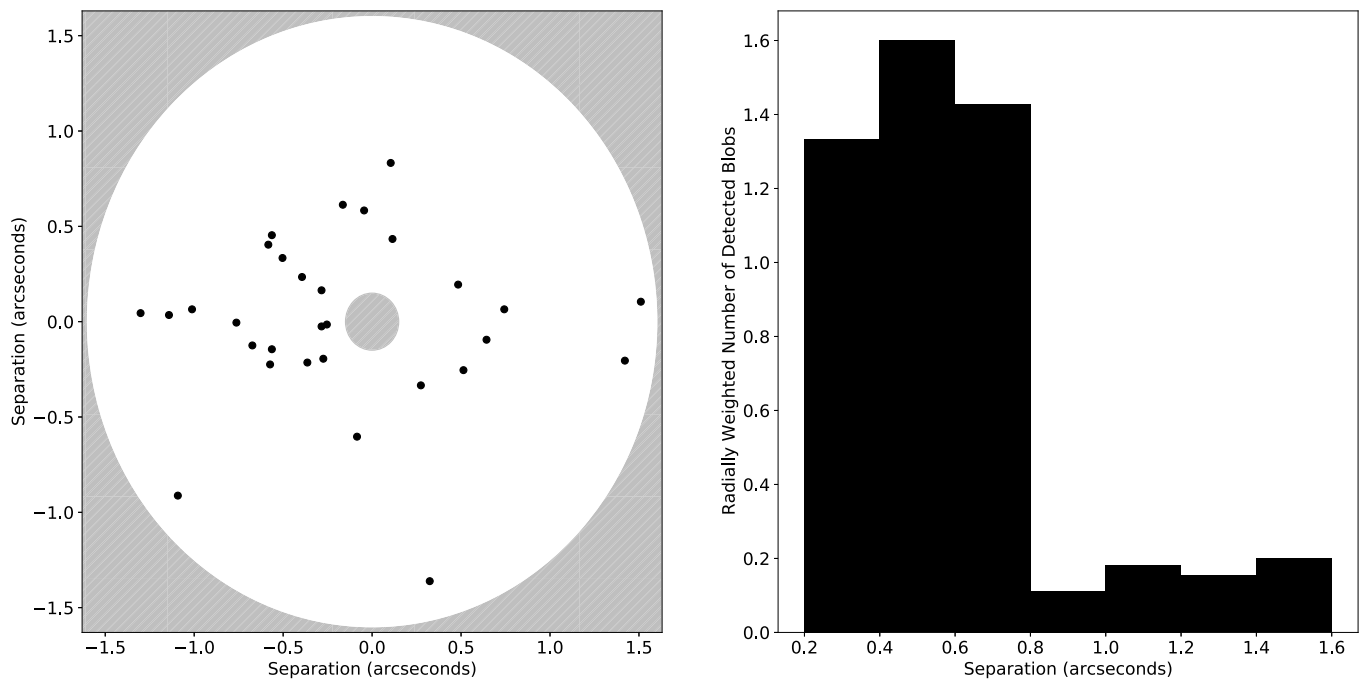

Figure C1. Left: Locations of all point sources detected in our observations with $S/N > 5$. The central 0″15 and separations >1″6 are hatched and represent the regions where we do not search for point sources. The clustering of points in radial lines is likely due to diffraction from the telescope support structure. Right: A histogram, weighted by area, of the separations of the detected point sources.

Appendix D
Age-independent Mass Estimates

The ages of young stars are notoriously difficult to ascertain. In Figures 5–10, we utilize our best isochrone-determined ages when estimating our planetary mass limits. Here, in Figures D1–D3, we show our gap and cavity mass plots for a variety of system ages.
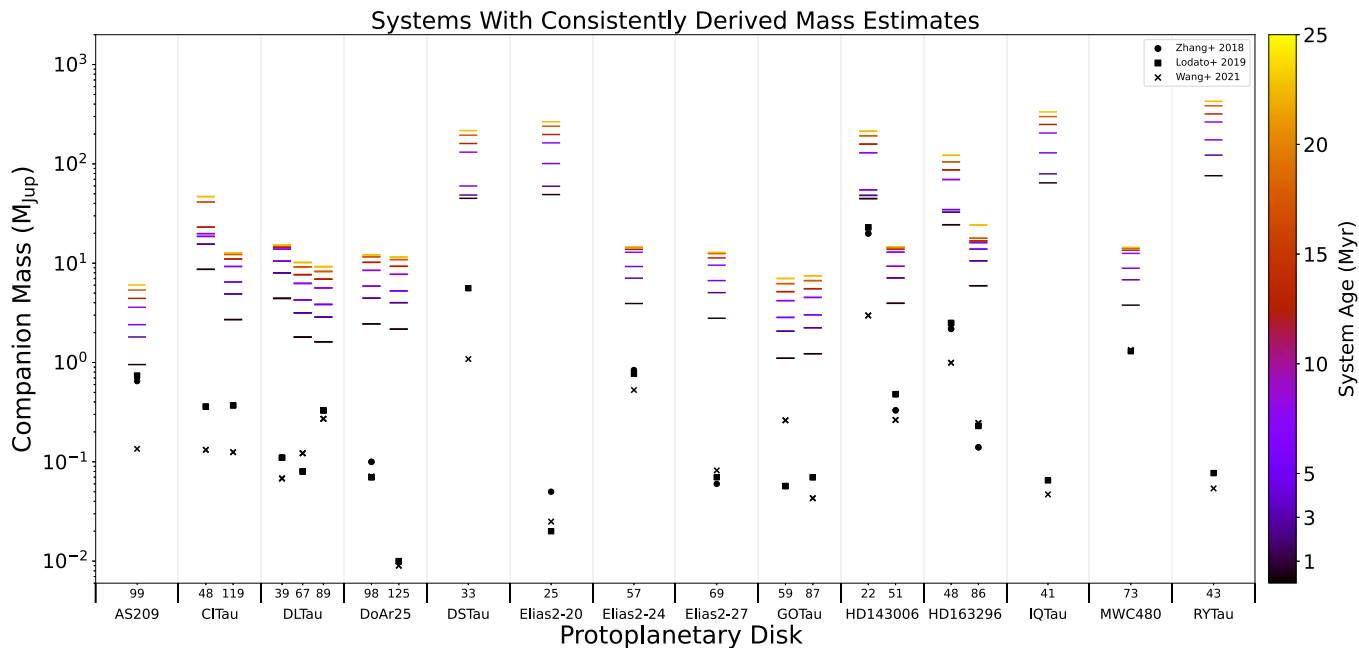

Figure D1. Similar to Figure 5, but showing the mass estimates derived from our 5σ contrast curves for a number of different system ages for systems observed as part of the DSHARP survey (Andrews et al. 2018) or the survey of the Taurus molecular cloud (Long et al. 2018). We show the ALMA-derived planet masses (in $M_{\rm Jup}$) as the points with our mass estimates using the AMES-Cond model shown as bars colored by system age. We specify the radial locations of the gaps that we are probing as numbers (in au) above each system name.
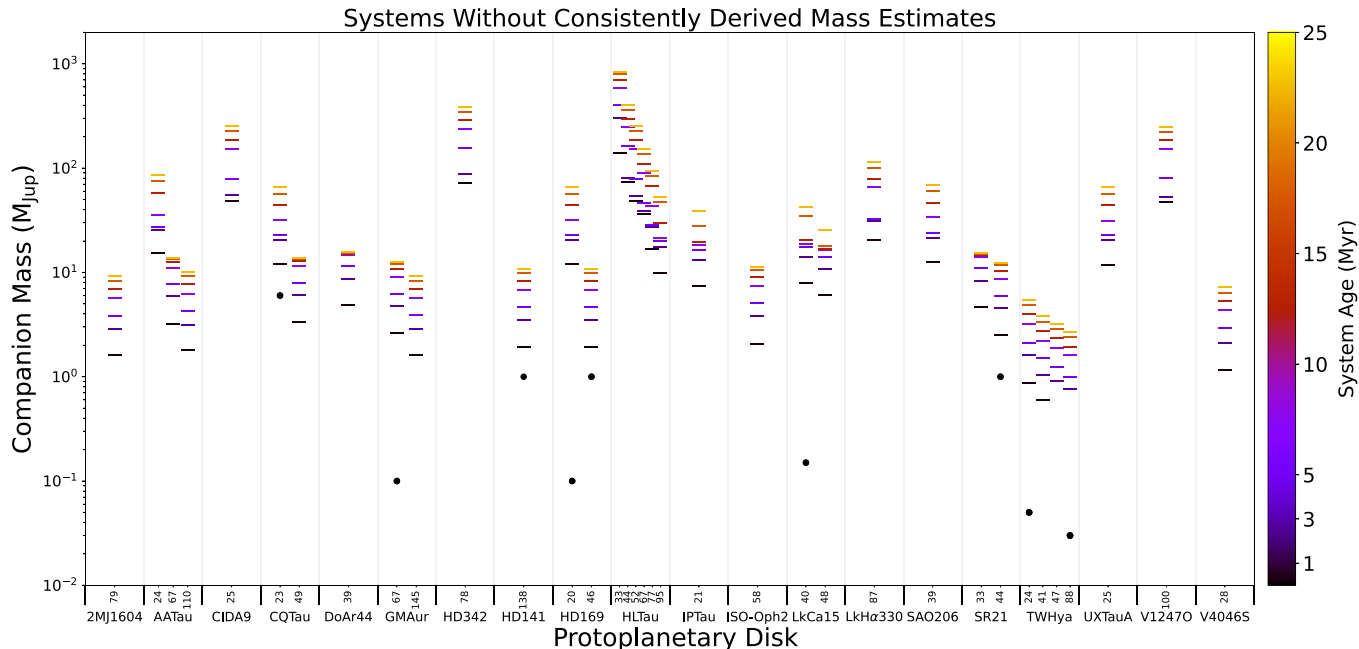
Figure D2. Similar to Figure 6, but showing the mass estimates derived from our 5σ contrast curves for a number of different system ages. We show our mass estimates using the AMES-Cond model as bars colored by system age. We specify the radial locations of the gaps that we are probing as numbers (in au) above each system name. When ages produce mass limits outside of the AMES-Cond model grid, we do not show those limits.
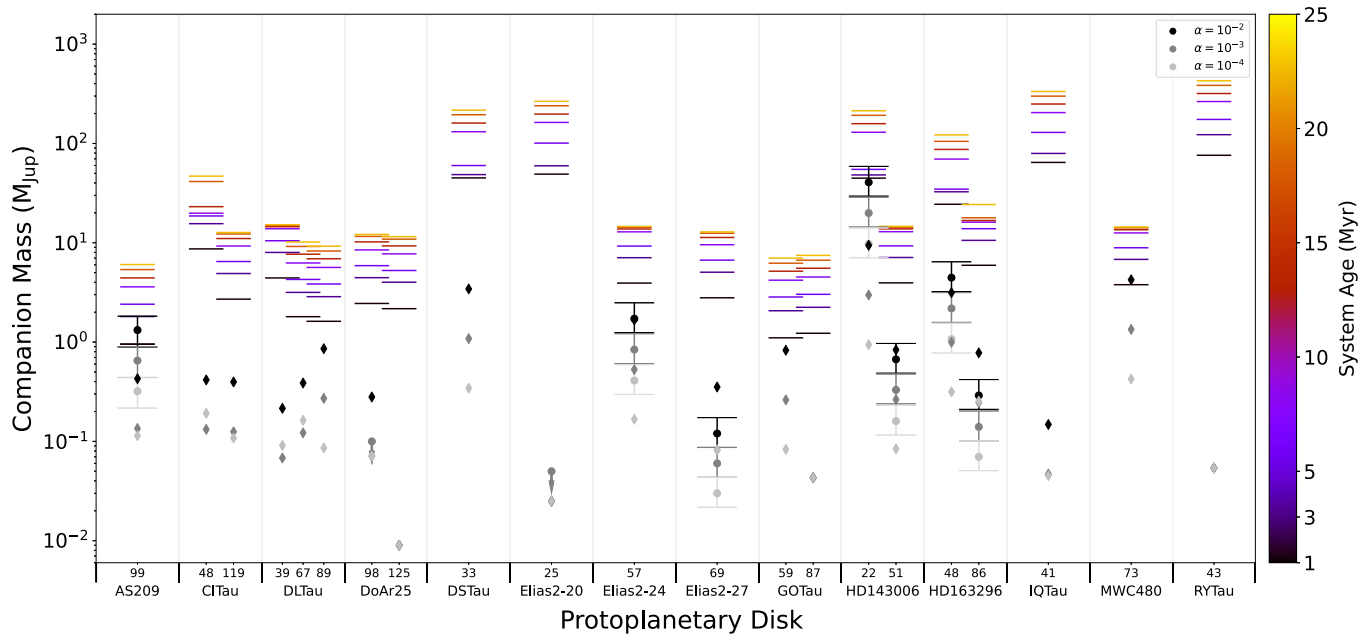
Figure D3. Similar to Figure 9, expected planet masses from Wang et al. (2021; diamonds with no associated errors as none were reported) and Zhang et al. (2018; circles with their associated errors) for the subset of our systems observed as part of the DSHARP survey (Andrews et al. 2018) or the survey of the Taurus molecular cloud (Long et al. 2018) calculated using different values for the disk viscosity, α, are shown as black and gray points. We show the planet mass estimates derived from our 5σ contrast limits for comparison using the AMES-Cond models (Baraffe et al. 2003).

ORCID iDs

Nicole L. Wallack ● https://orcid.org/0000-0003-0354-0187
Jean-Baptiste Ruffio ● https://orcid.org/0000-0003-2233-4821
Garreth Ruane ● https://orcid.org/0000-0003-4769-1665
Bin B. Ren (任彬) ● https://orcid.org/0000-0003-1698-9696
Jerry W. Xuan ● https://orcid.org/0000-0002-6618-1137
Marion Villenave ● https://orcid.org/0000-0002-8962-448X
Dimitri Mawet ● https://orcid.org/0000-0002-8895-4735
Karl Stapelfeldt ● https://orcid.org/0000-0002-2805-7338
Jason J. Wang ● https://orcid.org/0000-0003-0774-6502
Michael C. Liu ● https://orcid.org/0000-0003-2232-7664
Olivier Absil ● https://orcid.org/0000-0002-4006-6237
Jaehan Bae ● https://orcid.org/0000-0001-7258-770X
Michael Bottom ● https://orcid.org/0000-0003-1341-5531
Benjamin Calvin ● https://orcid.org/0000-0003-4737-5486
Élodie Choquet ● https://orcid.org/0000-0002-9173-0740
Valentin Christiaens ● https://orcid.org/0000-0002-0101-8814
Greta Guidi ● https://orcid.org/0000-0002-7002-8928
Joel Kastner ● https://orcid.org/0000-0002-3138-8250
Heather A. Knutson ● https://orcid.org/0000-0002-5375-4725
Tiffany Meshkat ● https://orcid.org/0000-0001-6126-2467
Henry Ngo ● https://orcid.org/0000-0001-5172-4859
Maddalena Reggiani ● https://orcid.org/0000-0003-2911-0898
Luca Ricci ● https://orcid.org/0000-0001-8123-2943
Taichi Uyama ● https://orcid.org/0000-0002-6879-3030
Jonathan P. Williams ● https://orcid.org/0000-0001-5058-695X
Peter Wizinowich ● https://orcid.org/0000-0002-1646-442X
Shangjia Zhang ● https://orcid.org/0000-0002-8537-9114
Zhaohuan Zhu ● https://orcid.org/0000-0003-3616-6822

References

Allard, F., Homeier, D., Freytag, B., & Sharp, C. M. 2012, in EAS Publ. Ser. 57, Low-Mass Stars and the Transition Stars/Brown Dwarfs, ed. C. Reylé, C. Charbonnel, & M. Schultheis (Les Ulis: EDP Sciences), 3
Andrews, S. M., Huang, J., Pérez, L. M., et al. 2018, ApJL, 869, L41
Andrews, S. M., Rosenfeld, K. A., Kraus, A. L., & Wilner, D. J. 2013, ApJ, 771, 129
Andrews, S. M., Wilner, D. J., Espaillat, C., et al. 2011, ApJ, 732, 42
Asensio-Torres, R., Henning, T., Cantalloube, F., et al. 2021, A&A, 652, A101
Baraffe, I., Chabrier, G., Barman, T. S., Allard, F., & Hauschildt, P. H. 2003, A&A, 402, 701
Benisty, M., Bae, J., Facchini, S., et al. 2021, ApJL, 916, L2
Benisty, M., Juhász, A., Facchini, S., et al. 2018, A&A, 619, A171
Boehler, Y., Ricci, L., Weaver, E., et al. 2018, ApJ, 853, 162
Bonavita, M., 2020 Exo-DMC: Exoplanet Detection Map Calculator, Astrophysics Source Code Library, ascl:2010.008
Bond, C. Z., Cetre, S., Lilley, S., et al. 2020, JATIS, 6, 039003
Carpenter, J. M., Ricci, L., & Isella, A. 2014, ApJ, 787, 42
Carrasco-González, C., Sierra, A., Flock, M., et al. 2019, ApJ, 883, 71
Choi, J., Dotter, A., Conroy, C., et al. 2016, ApJ, 823, 102
Cieza, L. A., González-Ruilova, C., Hales, A. S., et al. 2021, MNRAS, 501, 2934
Cugno, G., Pearce, T. D., Launhardt, R., et al. 2023, A&A, 669, A145
Currie, T., Marois, C., Cieza, L., et al. 2019, ApJL, 877, L3
Dong, R., & Fung, J. 2017, ApJ, 835, 146
Dong, R., Liu, S.-y., Eisner, J., et al. 2018, ApJ, 860, 124
Fedele, D., Carney, M., Hogerheijde, M. R., et al. 2017, A&A, 600, A72
Flaherty, K. M., Hughes, A. M., Teague, R., et al. 2018, ApJ, 856, 117
Flasseur, O., Thé, S., Denis, L., Thiébaut, É., & Langlois, M. 2021, A&A, 651, A62
Follette, K. B., Close, L. M., Males, J. R., et al. 2023, AJ, 165, 225
Gaia Collaboration, Brown, A. G. A., Vallenari, A., et al. 2021, A&A, 649, A1
Galli, P. A. B., Loinard, L., Ortiz-Léon, G. N., et al. 2018, ApJ, 859, 33
Gomez Gonzalez, C. A., Wertz, O., Absil, O., et al. 2017, AJ, 154, 7
González-Ruilova, C., Cieza, L. A., Hales, A. S., et al. 2020, ApJL, 902, L33
Guidi, G., Ruane, G., Williams, J. P., et al. 2018, MNRAS, 479, 1505
Guzmán-Díaz, J., Mendigutía, I., Montesinos, B., et al. 2021, A&A, 650, A182
Haffert, S. Y., Bohn, A. J., de Boer, J., et al. 2019, NatAs, 3, 749
Herczeg, G. J., & Hillenbrand, L. A. 2014, ApJ, 786, 97
Huang, J., Andrews, S. M., Dullemond, C. P., et al. 2020, ApJ, 891, 48
Huby, E., Bottom, M., Femenia, B., et al. 2017, A&A, 600, A46
Isella, A., Guidi, G., Testi, L., et al. 2016, PhRvL, 117, 251101
Isella, A., Pérez, L. M., & Carpenter, J. M. 2012, ApJ, 747, 136
Keppler, M., Benisty, M., Müller, A., et al. 2018, A&A, 617, A44
Keppler, M., Teague, R., Bae, J., et al. 2019, A&A, 625, A118
Kim, K. H., Watson, D. M., Manoj, P., et al. 2013, ApJ, 769, 149
Kluska, J., Kraus, S., Davies, C. L., et al. 2018, ApJ, 855, 44

Konishi, M., Grady, C. A., Schneider, G., et al. 2016, ApJL, 818, L23
Kraus, A. L., & Ireland, M. J. 2011, ApJ, 745, 5
Kraus, S., Ireland, M. J., Sitko, M. L., et al. 2013, ApJ, 768, 80
Kraus, S., Kreplin, A., Fukugawa, M., et al. 2017, ApJL, 848, L11
Kurtovic, N. T., Pérez, L. M., Benisty, M., et al. 2018, ApJL, 869, L44
Kwon, W., Looney, L. W., Mundy, L. G., & Welch, W. J. 2015, ApJ, 808, 102
Launhardt, R., Henning, T., Quirrenbach, A., et al. 2020, A&A, 635, A162
Liu, M. C. 2004, Sci, 305, 1442
Liu, S.-F., Jin, S., Li, S., Isella, A., & Li, H. 2018, ApJ, 857, 87
Lodato, G., Dipierro, G., Ragusa, E., et al. 2019, MNRAS, 486, 453
Long, F., Pinilla, P., Herczeg, G. J., et al. 2018, ApJ, 869, 17
Loomis, R. A., Öberg, K. I., Andrews, S. M., & MacGregor, M. A. 2017, ApJ, 840, 23
Mamajek, E. E., & Bell, C. P. M. 2014, MNRAS, 445, 2169
Manara, C. F., Testi, L., Natta, A., & Alcalá, J. M. 2015, A&A, 579, A66
Marocco, F., Eisenhardt, P. R. M., Fowler, J. W., et al. 2021, ApJS, 253, 8
Marois, C., Lafrenière, D., Doyon, R., Macintosh, B., & Nadeau, D. 2006, ApJ, 641, 556
Mawet, D., Choquet, É., Absil, O., et al. 2017, AJ, 153, 44
Mawet, D., Milli, J., Wahhaj, Z., et al. 2014, ApJ, 792, 97
McCarthy, K., & White, R. J. 2012, AJ, 143, 134
Meeus, G., Montesinos, B., Mendigutía, I., et al. 2012, A&A, 544, A78
Menu, J., van Boekel, R., Henning, T., et al. 2015, A&A, 581, A107
Muro-Arena, G. A., Ginski, C., Dominik, C., et al. 2020, A&A, 636, L4
Nomura, H., Tsukagoshi, T., Kawabe, R., et al. 2016, ApJL, 819, L7
Ohashi, S., & Kataoka, A. 2019, ApJ, 886, 103
Paardekooper, S. J., & Mellema, G. 2006, A&A, 453, 1129
Pairet, B., Cantalloube, F., & Jacques, L. 2021, MNRAS, 503, 3724
Pascucci, I., Testi, L., Herczeg, G. J., et al. 2016, ApJ, 831, 125
Pinilla, P., van der Marel, N., Pérez, L. M., et al. 2015, A&A, 584, A16
Pinte, C., van der Plas, G., Ménard, F., et al. 2019, NatAs, 3, 1109
Quiroz, J., Wallack, N. L., Ren, B., et al. 2022, ApJL, 924, L4
Rich, E. A., Wisniewski, J. P., Mayama, S., et al. 2015, AJ, 150, 86
Rosenfeld, K. A., Andrews, S. M., Wilner, D. J., & Stempels, H. C. 2012, ApJ, 759, 119

Rosenfeld, K. A., Andrews, S. M., Wilner, D. J., Kastner, J. H., & McClure, M. K. 2013, ApJ, 775, 136
Ruane, G., Mawet, D., Kastner, J., et al. 2017, AJ, 154, 73
Ruane, G., Ngo, H., Mawet, D., et al. 2019, AJ, 157, 118
Ruffio, J.-B., Macintosh, B., Wang, J. J., et al. 2017, ApJ, 842, 14
Sanchis, E., Picogna, G., Ercolano, B., Testi, L., & Rosotti, G. 2020, MNRAS, 492, 3440
Serabyn, E., Huby, E., Matthews, K., et al. 2017, AJ, 153, 43
Skemer, A. J., Marley, M. S., Hinz, P. M., et al. 2014, ApJ, 792, 17
Stone, J. M., Skemer, A. J., Hinz, P. M., et al. 2018, AJ, 156, 286
Szulágyi, J., Dullemond, C. P., Pohl, A., & Quanz, S. P. 2019, MNRAS, 487, 1248
Teague, R., Bae, J., Bergin, E. A., Birnstiel, T., & Foreman-Mackey, D. 2018, ApJL, 860, L12
Testi, L., Natta, A., Shepherd, D. S., & Wilner, D. J. 2003, A&A, 403, 323
Ubeira Gabellini, M. G., Miotello, A., Facchini, S., et al. 2019, MNRAS, 486, 4638
Uyama, T., Ren, B., Mawet, D., et al. 2020, AJ, 160, 283
van der Marel, N., Dong, R., di Francesco, J., Williams, J. P., & Tobin, J. 2019, ApJ, 872, 112
van der Marel, N., van Dishoeck, E. F., Bruderer, S., et al. 2016, A&A, 585, A58
van der Plas, G., Ménard, F., Canovas, H., et al. 2017, A&A, 607, A55
Villenave, M., Stapelfeldt, K. R., Duchêne, G., et al. 2022, ApJ, 930, 11
Wang, J. J., Ginzburg, S., Ren, B., et al. 2020, AJ, 159, 263
Wang, J. J., Ruffio, J.-B., De Rosa, R. J., et al., 2015 pyKLIP: PSF Subtraction for Exoplanets and Disks, Astrophysics Source Code Library, ascl:1506.001
Wang, S., Kanagawa, K. D., & Suto, Y. 2021, ApJ, 923, 165
Weidenschilling, S. J. 1977, MNRAS, 180, 57
Wölfer, L., Facchini, S., Kurtovic, N. T., et al. 2021, A&A, 648, A19
Xuan, W. J., Mawet, D., Ngo, H., et al. 2018, AJ, 156, 156
Zhang, K., Isella, A., Carpenter, J. M., & Blake, G. A. 2014, ApJ, 791, 42
Zhang, S., Zhu, Z., Huang, J., et al. 2018, ApJL, 869, L47
Zhu, Z. 2015, ApJ, 799, 16
Zhu, Z., Stone, J. M., Rafikov, R. R., & Bai, X.-N. 2014, ApJ, 785, 122